Journal of Hazardous Materials 191 (2011) 306–324

Contents lists available at ScienceDirect

Journal of Hazardous Materials

journal homepage: www.elsevier.com/locate/jhazmat

Predictive hydrogeochemical modelling of bauxite residue sand in field conditions

Laurin Wissmeier[a,*], David A. Barry[a], Ian R. Phillips[b]

[a] Ecole Polytechnique Fédérale de Lausanne (EPFL), Faculté de l'Environnement Naturel, Architectural et Construit (ENAC), Laboratoire de Technologie Ecologique, Station 2, 1015 Lausanne, Switzerland
[b] Mining Environmental Group, Alcoa of Australia Ltd., PO Box 172, Pinjarra, WA 6208, Australia

ARTICLE INFO

Article history:
Received 23 July 2010
Received in revised form 15 April 2011
Accepted 18 April 2011
Available online 23 April 2011

Keywords:
Bauxite refining residue
Geochemical modelling
IPhreeqc
COMSOL
Vadose zone
Waste management

ABSTRACT

The suitability of residue sand (the coarse fraction remaining from Bayer's process of bauxite refining) for constructing the surface cover of closed bauxite residue storage areas was investigated. Specifically, its properties as a medium for plant growth are of interest to ensure residue sand can support a sustainable ecosystem following site closure. The geochemical evolution of the residue sand under field conditions, its plant nutrient status and soil moisture retention were studied by integrated modelling of geochemical and hydrological processes. For the parameterization of mineral reactions, amounts and reaction kinetics of the mineral phases natron, calcite, tricalcium aluminate, sodalite, muscovite and analcime were derived from measured acid neutralization curves. The effective exchange capacity for ion adsorption was measured using three independent exchange methods. The geochemical model, which accounts for mineral reactions, cation exchange and activity corrected solution speciation, was formulated in the geochemical modelling framework PHREEQC, and partially validated in a saturated-flow column experiment. For the integration of variably saturated flow with multi-component solute transport in heterogeneous 2D domains, a coupling of PHREEQC with the multi-purpose finite-element solver COMSOL was established. The integrated hydrogeochemical model was applied to predict water availability and quality in a vertical flow lysimeter and a cover design for a storage facility using measured time series of rainfall and evaporation from southwest Western Australia. In both scenarios the sand was fertigated and gypsum-amended. Results show poor long-term retention of fertilizer ions and buffering of the pH around 10 for more than 5 y of leaching. It was concluded that fertigation, gypsum amendment and rainfall leaching alone were insufficient to render the geochemical conditions of residue sand suitable for optimal plant growth within the given timeframe. The surface cover simulation demonstrates that the soil moisture status in the residue sand can be ameliorated by an appropriate design of the cover layer with respect to thickness, slope and distance between lateral drains.

1. Introduction

The worldwide production of alumina (83.3 Mt in 2008 [1]) is associated with the creation of about 120 Mt of problematic bauxite refining residues each year [2]. In Western Australia, where about a third of the alumina on the global market is produced [3], the residue is disposed of in large impoundments close to the refineries, where it is left to drain and air-dry (dry-stacking) [4,5]. In anticipation of future storage capacity limits, the bauxite refining industry seeks safe and economically feasible strategies of sustainable storage site closure. Important objectives for successful closure are [6–11]:

- reduction of infiltration into the underlying residue;
- dust control;
- erosion control;
- minimization of the need for future reworking; and,
- limitation of the visual obtrusiveness.

These objectives could be achieved by a self-sustaining vegetation cover on top of residue storage areas. Since the reuse of residue sand (the coarse fraction of the residue; characteristic grain size $>10^{-4}$ m) as a medium for plant growth would greatly reduce the costs of revegetation, research into its suitability as a substrate has been recently intensified. However, plant productivity on residue sand is impeded by the geochemical conditions that reactions of highly unstable minerals impose on the soil solution [12]. Characteristic properties of the residue sand are [7,11,13–15]:

- high pH (10–12.5);

* Corresponding author. Tel.: +49 761 211 1380; fax: +49 761 211 138 29.
E-mail addresses: laurin.wissmeier@epfl.ch (L. Wissmeier), andrew.barry@epfl.ch (D.A. Barry), ian.phillips@alcoa.com.au (I.R. Phillips).

0304-3894/$ – see front matter © 2011 Elsevier B.V. All rights reserved.
doi:10.1016/j.jhazmat.2011.04.078

- high total alkalinity (ca. 20 meq l^{-1});
- high electrical conductivity (ca. 1500 $\mu S\,cm^{-1}$); and,
- high exchangeable sodium percentage (close to 100%).

Besides the general geochemical conditions, the plant nutrient status in the residue sand plays a critical role for the long-term revegetation success [8,12,15]. Chen et al. [16,17] therefore investigated the retention of major nutrients in residue sand after additions of a standard ammonium-phosphate fertilizer. In [17], they specifically focused on the loss of ammonia (NH_3) due to volatilization. Fractionation and availability of micronutrients such as B, Cu, Fe, Mn and Zn in residue sand was examined by Thiyagarajan et al. [10]. Motivated by the observed Mn deficiency of plants on residue sand, Gherardi and Rengel [13] investigated the detailed fractionation of this essential nutrient. Phillips and Chen [14] studied ion adsorption onto variable charge adsorption sites as the main fractionating process for micronutrients.

To date the interference on adsorption sites of fertilizer retention and mineral dissolution reactions as result of ion competition remains unclear. More importantly, the influence of soil moisture dynamics and solute transport on the geochemical factors that determine sand fertility in field conditions is largely unknown. Under natural leaching conditions, imposed by rainfall and evaporation, geochemical processes of ion adsorption and mineral dissolution are controlled by variably saturated soil moisture movement and influenced by changes in local ion concentrations due to solute transport [18–21]. Therefore, flow and transport are crucial components in the assessment of the long-term efficiency of management strategies, such as fertilizer addition or gypsum amendment [22–24]. Besides its importance for ion transport and solution reactivity, water availability plays a key role in residue sand fertility.

Integrated hydrogeochemical modelling is a powerful tool to investigate simultaneous geochemical reactions, such as mineral reactions and ion adsorption, considering their dependency on soil moisture dynamics and solute transport [25–28]. Here, we present the first interdisciplinary modelling of bauxite refining residue sand by combining geochemical reactions with rainfall- and evaporation-induced variably saturated flow in 2D heterogeneous domains. The objectives are (1) to develop and parameterize submodels for the geochemical and hydrological processes in residue sand, and (2) to predict the long-term effect of fertilization and gypsum amendment on residue sand fertility in field conditions through integrated hydrogeochemical modelling.

The paper is structured as follows: A geochemical model for residue sand is established in Section 2. Mineral reactions are derived from measured acid neutralization curves in combination with speciation modelling and linked parameter optimization. Ion adsorption is considered by a cation exchange process using independent measurements to determine the effective exchange capacity. The model is formulated in the geochemical modelling framework PHREEQC [29] and is partially validated against results from saturated-flow column experiments. Section 3 presents the hydraulic properties of residue sand with relevance to hydrological modelling. The software for coupled simulations of geochemistry and unsaturated hydrological processes is described briefly in Section 4. Details of novel model features and the implementation of atmospheric boundary conditions are provided in Appendices A–C. Section 5 describes the meteorological conditions at ALCOA's Pinjarra Alumina Refinery in south-west Western Australia where the model is applied. Results from predictive simulations of a constructed lysimeter and a surface cover design for residue storage areas are presented in Sections 6 and 7. The main model uncertainties are discussed in Section 8 together with implications for residue management. Conclusions with respect to the fertilizer addition and gypsum amendment as well as the overall suitability of residue sand as a plant growth substrate are drawn in Section 9.

2. Geochemical model

2.1. Solid phase properties

The geochemistry of fresh, untreated residue sand is dominated by dissolution of readily soluble salts and minerals [30]. In order to simulate the geochemical conditions as a response to fertigation, gypsum amendment and rainfall leaching, detailed knowledge of the stoichiometry, quantity and reactivity of the soluble minerals is required. Taylor and Pearson [31] found 58% quartz, 22% hematite, 7% gibbsite, 5% goethite, 1% anatase, 1% muscovite and 0.3% boehmite as the major mineral fractions in residue sand. Because of their low solubility and/or slow reactions kinetics, these major mineral fractions contribute little to the overall geochemical conditions in the soil solution. Instead, highly reactive salts such as natron ($Na_2CO_3{:}10H_2O$), calcite ($CaCO_3$), tricalcium aluminate (TCA; $Ca_3Al_2O_6$) [32–34] and the desilication product (DSP; e.g., sodalite $Na_8(AlSiO_4)_6Cl_2$) [15,35–40] are responsible for the high pH and large acid neutralization capacity of the bauxite residue [30,41]. Although identified qualitatively by XRD [30], the proportions of these minerals in residue sand are currently unknown.

For the parameterization of the geochemical model, the reactive mineral proportions were found by matching measured acid neutralization curves with simulations performed in PHREEQC. In this approach, the solution pH was regarded as a master variable and an integrated measure for the overall geochemical conditions [42]. Similar to the procedure used by Snars and Gilkes [30], buffering plateaus are associated with the dissolution of distinct mineral phases and the persistence of buffering regions is related to the amount of the minerals in the mineral assembly.

Acid neutralization was measured over the pH range of 2–12. 30 g of residue sand ($\varnothing < 2$ mm, oven-dried for >2 d at 50 °C) were placed into a series of 20 polystyrol screw-lid beakers (190 ml, Semadeni). A 0.5 M HCl solution was added to the beakers in quantities ranging from 0 to 14.25 ml in steps of 0.75 ml. The beakers were made up to volume using Milli-Q deionised water to achieve a liquid to solid ratio of 5:1 by weight. Samples were thoroughly mixed (20 rpm) using an end-over-end shaker. Excessive gas phase equilibration was avoided by reducing the empty volume in each beaker to ca. 20 ml. The pH of each suspension was recorded 2, 4, 24, 48, 72 and 96 h after acid addition using a robotic titrosampler (Metrohm 855) with a platinum electrode (Metrohm 6.0257.000 Aquatrode Plus).

Acid neutralization curves show distinct buffering plateaus at pH 7 and pH 4 and a less pronounced buffering region around pH 9–10 (Fig. 1a). Over time, acid consumption increased due to kinetic mineral dissolution, giving the impression of a moving pH front. After 72 h, the pH stabilized, suggesting that readily soluble alkalinity was consumed and that fast kinetic reactions attained quasi-equilibrium. The extent of further buffering due to slowly reacting minerals remains uncertain. However, over the time scale examined, the acid neutralization curves provide reliable information on the effects of acid on the geochemical behaviour of residue sand.

In the first step of the model development, the acid neutralization at 2 h was reproduced by simulating the solution in equilibrium with the fast reacting minerals natron, calcite, muscovite and analcime. The latter two minerals provide buffering around pH 4 and are therefore of minor importance under conditions typically observed for residue sand deposited in the field (pH > 7). The quantity of natron and calcite were optimized to match the measured acid neutralization curve through coupling PHREEQC with the model-

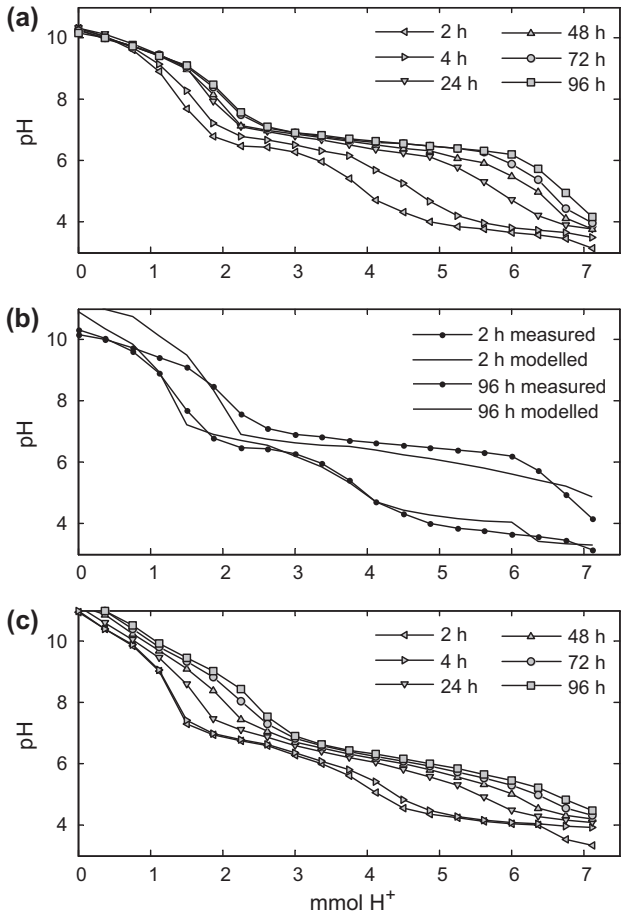

Fig. 1. Measured (a) and simulated acid neutralization curves at thermodynamic equilibrium (b) and including the kinetic dissolution of TCA and sodalite (c).

independent parameter estimation software PEST (version 12) [43]. The second step in model development introduced the minerals TCA and sodalite, whose quantities were optimized in PHREEQC to reproduce the acid neutralization curve observed after 96 h of reaction time. The mineral sodalite was included as a surrogate to represent the variety of components in the desilication product [44]. Similarly, TCA represents the mineral group of calcium aluminates. Since the buffering capacity around pH 4 was not exhausted during the experiment, the amount of muscovite was estimated from the mineralogical data of Taylor and Pearson [31] given above. The amount of sodium (Na) in fresh residue sand that is not accounted for by natron and sodalite was attributed to analcime. Reactive Na as measured by leach testing over a range of pH from 0.8 to 11.8 (data not shown) amounts to 5.415×10^{-3} g g^{-1}. Measured and simulated acid neutralization curves at 2 and 96 h are presented in Fig. 1b. In a third step of model development, acid neutralization between 2 and 96 h was attributed to kinetic dissolution of TCA and sodalite. In agreement with transition state theory [45], the rate expression

$$S_i \frac{dm_i}{dt} = k(1-\Omega)A\left(\frac{M}{M_0}\right)^{2/3}, \quad (1)$$

given by the PHREEQC manual [29] was employed. In Eq. (1), s_i is the stoichiometric factor of component i in the mineral phase, m_i is the quantity of component i in the liquid phase (mol), k is the rate constant (mol m^{-2} s^{-1}), Ω is the saturation ratio and A is the mineral surface area (m^2). The factor $(M/M_o)^{2/3}$ accounts for the change in mineral surface with dissolution progress for spherical mineral grains, where M is the current amount of mineral (mol) and M_0 is the initial amount of mineral (mol). The saturation ratio Ω is defined by

$$\Omega = \frac{\Pi a_i^{s_i}}{K}, \quad (2)$$

where a_i is the activity of component i and K is the equilibrium constant of the dissolution/precipitation reaction. The reactive surface area A of the mineral phases was set equal to the total surface area of residue sand. The total surface area (2.708×10^{-2} m^2 g^{-1}) was calculated from laser diffraction particle analysis (LS^{TM} 13,320, Beckman Coulter) assuming spherical particles (Appendix D). The rate constant k and the initial amount M_0 were estimated by matching all measured acid neutralization curves at all time periods between 2 and 96 h of reaction by the coupling of PHREEQC and PEST (Fig. 1c).The derived mineral properties for subsequent modelling are summarized in Table 1.

The results in Fig. 1b show excellent agreement between the simulated and measured acid neutralization curves after 2 h using the fast reacting minerals natron and calcite to represent the buffering regions at pH 7 and around pH 10. The correlation coefficient according to Cooley and Naff [47] amounts to 0.995. The measured decline in pH with the addition of 2 mmol HCl as well as the exhaustion of the buffering capacity after addition of 7 mmol HCl is well reproduced. However, the pH is overestimated by about 1 pH unit in the strongly alkaline region (pH > 9), whereas it is slightly underestimated for the addition of 2–7 mmol acid. This is reflected also by the lower correlation coefficient of 0.973.The simulation of kinetic pH buffering in Fig. 1c, with an overall correlation coefficient of 0.982, shows that simple rate expressions are sufficient to produce reasonable agreement of this time-dependent process. Since the field pH remains always in the alkaline range, the mismatch between measured and simulated pH below 7 is of lower importance.

2.2. Adsorption properties

The adsorption of fertilizers as result of cation exchange is critical to the understanding of nutrient retention, which is crucial for plant growth. The effective cation exchange capacity (CEC) of residue was measured using three independent methods: (i) the method of Ca–Mg exchange for soils containing salts, carbonates and zeolites [48], (ii) the unbuffered salt extraction method at field pH (modified after [49], in [50]), and (iii) the cobalt hexamine compulsive exchange method [51]. Measurements were taken from three replicates using each method.

Prior to testing, the residue sand was washed to avoid errors due to the dissolution of readily soluble salts. 40 g of oven-dried sand (50 °C, >2 d, ø < 0.5 mm) were weighed into a 250 ml Nalgene bottle, after which 200 ml of water (Milli-Q) was added to achieve a liquid to solid ratio of 5:1. The bottles were shaken end-over-end for 1 h and centrifuged at 2×10^3 rpm for 30 min. The clear supernatant was manually decanted and care was taken not to lose any of the fine material that deposited as a red layer on top of the coarse sand. Subsequently, the bottles were made up to volume. The washing procedure was repeated 10 times, during which the electrical conductivity decreased from 1513 μS cm^{-1} to 53 μS cm^{-1} indicating the removal of the most soluble mineral fractions [52].

Each of the three methods yielded CEC values of the same order of magnitude (Table 2). However, the value from the NH_4–K exchange method was about twice as high as results from the other two methods. The Ca–Mg exchange method and the cobalt hexamine method lower the native pH of the residue sand. This may decrease the number of pH-dependent surface sites, which could explain the lower measured exchange capacity. In the following model applications the arithmetic mean of all three methods (CEC: 0.86 cmol kg$_{solid}^{-1}$) was used as the effective exchange capac-

Table 1
Mineral properties of residue sand as derived from acid neutralization.

Mineral name reaction formula	Equilibrium constant	Rate constant (mol m^{-2} s^{-1})	Relative amount (mol kg_{solid}^{-1})
Calcite $CaCO_3 = CO_3^{-2} + Ca^{+2}$	$10^{-8.48}$ [a]	–	2.531×10^{-2}
Natron $Na_2CO_3{:}10H_2O = 2Na^+ + CO_3^{-2} + 10H_2O$	$10^{-1.311}$ [a]	–	3.991×10^{-2}
Muscovite $KAl_3Si_3O_{10}(OH)_2 + 10H^+ = K^+ + 3Al^{+3} + 3H_4SiO_4$	10^{14} [b]	–	2.511×10^{-2}
Analcime $NaAlSi_2O_6{:}H_2O + H_2O + 4H^+ = Na^+ + Al^{+3} + 2H_4SiO_4$	$10^{6.719}$ [a]	–	3.054×10^{-2}
Sodalite $Na_8(AlSiO_4)_6Cl_2 + 24H_2O = 8Na^+ + 6Al(OH)_4^- + 6H_4SiO_4 + 2Cl^-$	$10^{-55.89}$ [c]	3.405×10^{-9}	4.237×10^{-3}
TCA $Ca_3Al_2O_6 + 12H^+ = 3Ca^{+2} + 2Al^{+3} + 6H_2O$	10^{74} [d]	7.484×10^{-10}	5.569×10^{-3}

[a] minteq.dat (distributed with PHREEQC).
[b] sit.dat (distributed with PHREEQC).
[c] Calculated from thermodynamic data in Komada et al. [46].
[d] Khaitan et al. [34].

Table 2
Cation exchange capacity on washed residue sand.

Method	CEC (cmol kg_{solid}^{-1})
(i) Ca–Mg	0.66
(ii) NH_4–K	1.21
(iii) $Co(NH_3)_6Cl_3$	0.72

ity of residue sand. For the definition of ion association reactions, PHREEQC's default database *phreeqc.dat* was employed.

2.3. Column study for model validation

Before modelling fertilizer transport under field conditions, the model representation of geochemical processes under controlled laboratory conditions was evaluated. A column leaching experiment in saturated upward flow conditions was performed to provide partial validation of the geochemical model by comparison of simulated and measured pH, electrical conductivity and element concentrations in the outflow. The experimental setup is displayed in Fig. 2.

In order to achieve homogenous packing, the untreated, oven-dried residue sand (50 °C, >2 d, ø < 2 mm) was poured into a glass column in portions of 5 ± 2 g while a head of 2–5 cm of Milli-Q water was maintained in the column [wet packing, [53]]. This packing achieved a final bulk density of about 1.56 g cm^{-3}. No particle separation was observed in the sand column after packing. Deionised water was supplied at the base (inflow) of the vertical column at a constant flux (15.03 cm^3 min^{-1}) using a peristaltic pump (Ismatec MCP). The discharge was collected above the outflow plug in 75.15 cm^3 aliquots, and retained for analysis. Column properties are shown in Table 3.

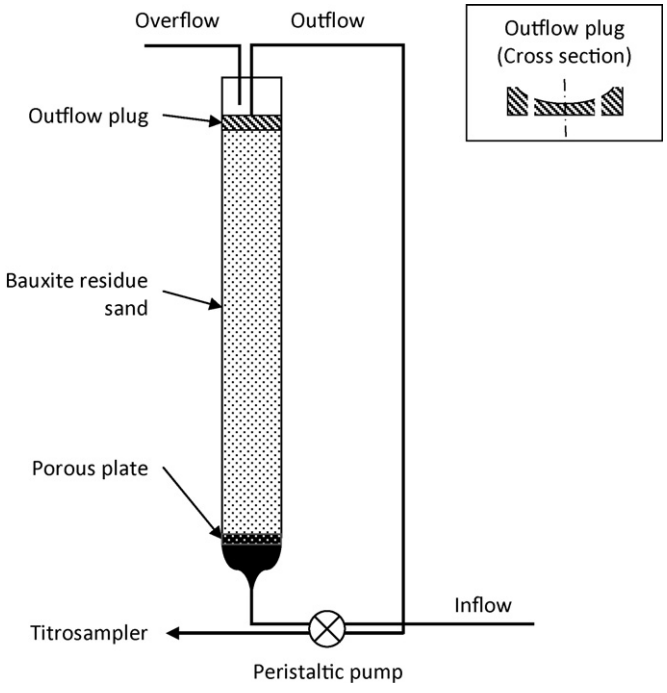

Fig. 2. Upward flow column experiment.

The leaching experiment was performed in three replicates (Series I, II and III). Automated measurements of pH and electrical conductivity in the outflow aliquots were taken using a robotic titrosampler (Metrohm 855 Robotic Titrosampler) in combination with appropriate electrodes (Metrohm 6.0257.000 Aquatrode Plus, Metrohm 712 Conductometer with Metrohm 6.0912.110). For alkalinity measurements, samples were immediately titrated to pH 4.3 with 0.01 M HCl using an automated titrator (Metrohm 800 Dosino). The CO_2 gas saturation was calculated from pH and alkalinity measurements using PHREEQC by attribution of alkalinity to carbonate species, protons and hydroxyl ions. Major element concentrations were measured in the outflow of Series III using an ICP-OES instrument (PerkinElmer Optima 3300 DV). Samples were filtered (Whatman Spartan 30 0.45 μm), acidified to pH < 2 using HCl and stored at 4 °C prior to analysis.

The column experiment was simulated using PHREEQC's 1D-transport capabilities and the geochemical properties that were derived in Sections 2.1 and 2.2. The initial pore water and the inflowing solution were assumed to be in equilibrium with atmospheric CO_2 and O_2. Ion diffusion and physical dispersivity were estimated as 3×10^{-10} m^2 s^{-1} and 10^{-1} m, respectively. Flushing the column with 100 pore volumes corresponds to approximately 35 y of rainfall leaching in the climatic conditions of Western Australia with an estimated annual effective recharge of 600 mm (Section 5). Measured and simulated pH, alkalinity, electrical conductivity (EC) and CO_2 saturation in the discharge are presented in Fig. 3. The pH buffering simulated with the suggested mineral assembly agrees well with observations (Fig. 3a). The overestimation of pH during the first few pore volumes can be attributed to the assumed thermodynamic equilibrium with natron. The simulation of electrical conductivity according to solution species mobility matches well the observations (Fig. 3c). Alkalinity (Fig. 3b), which mainly results from carbonate species, was overestimated by the model, possibly due to equilibration with calcite. Despite this, reasonable agreement for CO_2-saturation in the column simulation was achieved (Fig. 3d).

Table 3
Column properties.

Property	Value
Column diameter	40 mm
Column length	600 mm
Flux	15.03 cm^3 min^{-1}
Porosity	0.43
Fill volume	600 cm^3

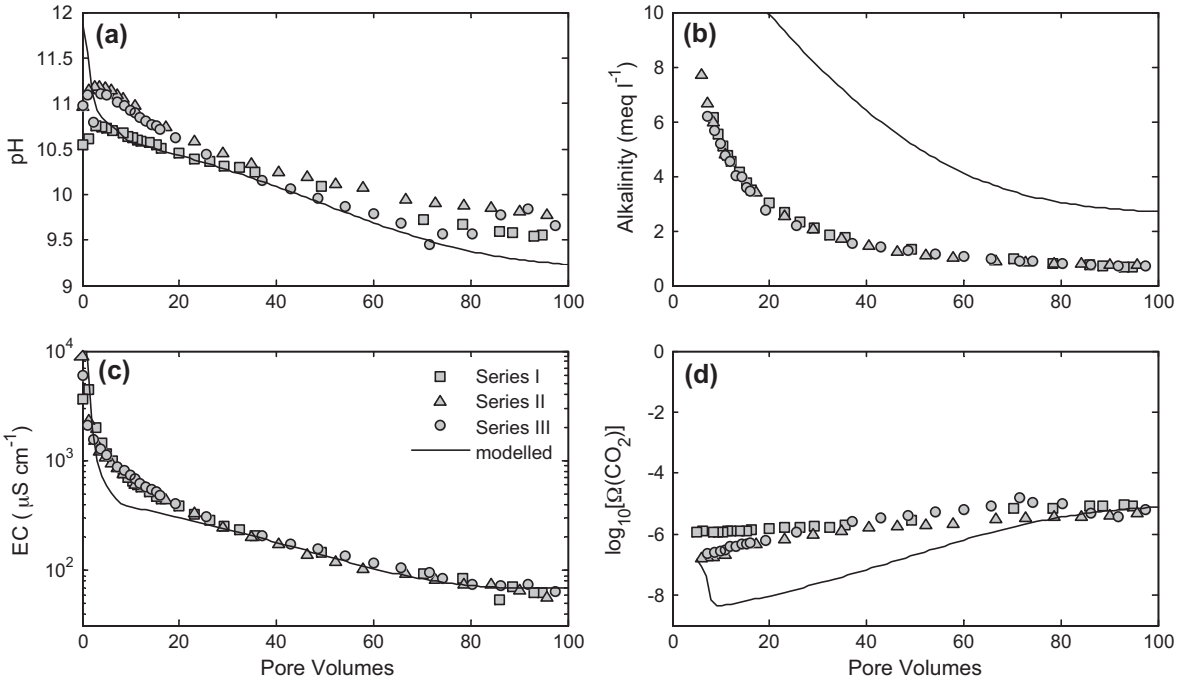

Fig. 3. Results of column experiment for pH (a), alkalinity (b), electrical conductivity (c) and calculated CO_2 saturation (d).

Results of the element analysis together with modelled total element concentrations in the column outflow are displayed in Fig. 4.

The simulation of Na concentrations in Fig. 4a agrees very well with observations. Concentrations of potassium (K) (Fig. 4b) are largely underestimated due to the low solubility of muscovite, which is the only source of K in the chosen mineral model. Aluminium (Al) concentrations in Fig. 4c are overestimated by an order of magnitude compared to measurements. This suggests too high solubility constants for DSP and TCA obtained from the literature or reprecipitation of Al in the form of aluminium oxides such as gibbsite and boehmite or aluminium silicates. The mismatch of Ca concentrations in Fig. 4d together with the overestimated alkalinity from Fig. 3b suggests that calcite may not be present as a pure phase, although it is modelled as such.

Overall, the comparison of measured and modelled drainage composition shows that large uncertainties exist in setting key mineralogical properties of residue sand. Despite these shortcomings, the geochemical model is considered suitable for estimating the geochemical evolution of residue sand in field conditions because it is capable of reproducing main geochemical features such as pH, EC and Na concentrations.

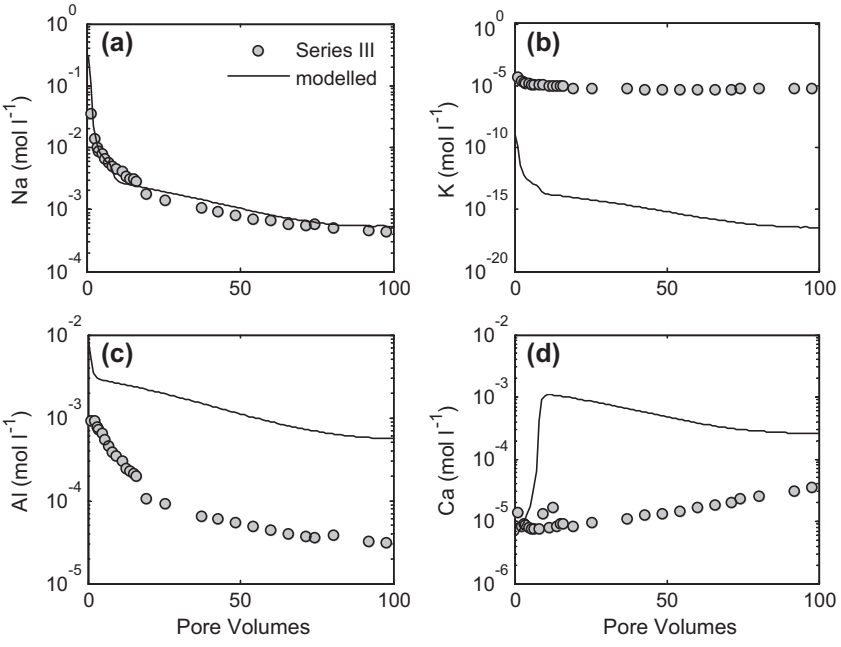

Fig. 4. Element concentrations (mol l^{-1}) in the column outflow for (a) Na, (b) K, (c) Al and (d) Ca.

3. Hydraulic model

For the hydraulic characterization of residue sand in variably saturated flow conditions the van Genuchten/Mualem model [54,55] for water retention and unsaturated hydraulic conductivity as in [56] was used. The van Genuchten function [55] is given by

$$\theta(h) = \begin{cases} \theta_r + \dfrac{\theta_s - \theta_r}{[1 + (\alpha h)^n]^m}, & h < 0, \\ \theta_s, & h \geq 0 \end{cases}, \quad (3)$$

where h is the pressure head (cm), θ is the actual moisture content, θ_r is the residual moisture content, θ_s is the saturated moisture content and α (cm^{-1}), n and m=1 − 1/n are soil-specific parameters. The free parameters were determined by fitting Eq. (3) to measurements of water retention that were taken in a pressure range of 0–15 bars using the RETC code [57].

Unsaturated hydraulic conductivity according to the Mualem model [54] is given by

$$K(\Theta) = K_s \Theta^l \left[1 - \left(1 - \Theta^{\frac{1}{m}}\right)^m\right]^2, \quad (4)$$

where Θ=$\theta - \theta_r/\theta_s - \theta_r$ is the reduced moisture content. The parameter l was taken as 0.5. The saturated hydraulic conductivity K_s ($m\,d^{-1}$) of the residue sand was measured in situ at various depths using a Guelph constant head permeameter. Its value at the soil surface was measured as 12.008 m d^{-1}. Measured values of water retention and the best fit of the van Genuchten function with parameters α=0.075 cm^{-1}, n=1.822, θ_s=0.454 and θ_r=0.039 are displayed together with unsaturated conductivity in Fig. 5.

Conductivity measurements suggest a non-linear relation between K_s and distance to the soil surface z (m) of the form:

$$K_s(z) = a \exp(bz) \quad (5)$$

which was fitted to the data using a least square criterion. The parameters a and b were determined as 12.008 m d^{-1} and −0.885 m^{-1}, respectively, with a coefficient of determination of 0.92.

The saturated water content θ_s up to a depth of 3 m was calculated from the measured θ_s at the surface and measured values of dry bulk density (1.3 g cm^{-3} at the surface versus 1.5 g cm^{-3} at 3 m depth). Assuming a constant solid density, a linear relation between depth and θ_s was established according to

$$\theta_s(z) = cz + d, \quad (6)$$

with c = 0.028 m^{-1} and d = 0.454. Depth-dependent measurements of K_s and θ_s together with the fitted Eqs. (5) and (6) are displayed in Fig. 6.

All other parameters in the van Genuchten/Mualem hydraulic model were assumed constant throughout the profile.

Transverse and longitudinal dispersivity in the residue sand were estimated as 10^{-1} m. For simplicity, the influences of water saturation [58,59] and scale [60] were neglected. The coefficient of molecular diffusion was taken as 3×10^{-10} $m^2\,s^{-1}$ according to the PHREEQC default settings (temperature of 25 °C).

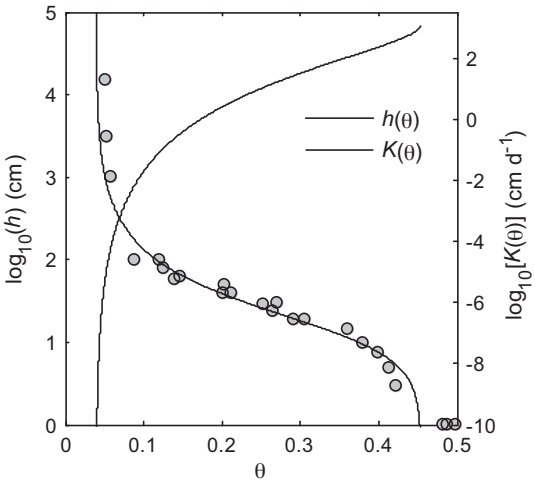

Fig. 5. Water retention and unsaturated hydraulic conductivity of residue sand at the soil surface according to the van Genuchten/Mualem model.

4. Software for integrated hydrogeochemical modelling

Processes of variably saturated liquid phase flow, multicomponent solute transport and geochemical reactions according to the geochemical and hydraulic properties described earlier were combined into an integrated hydrogeochemical model of bauxite

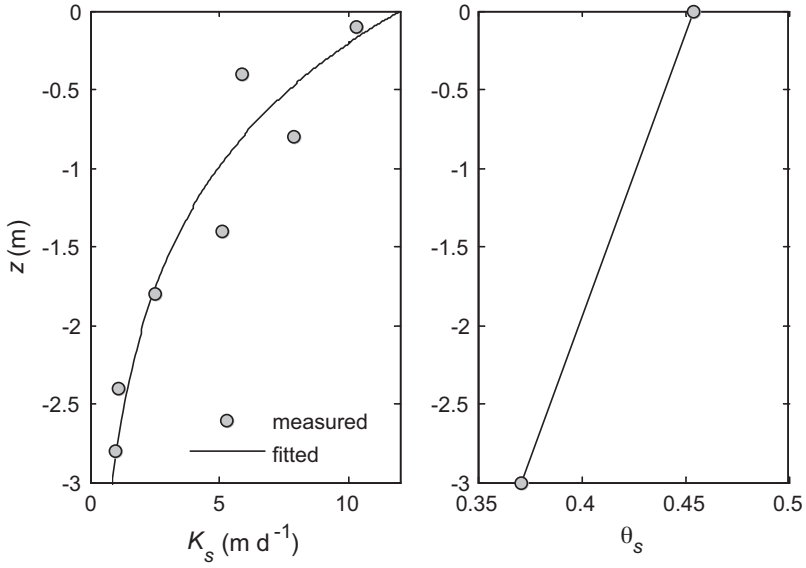

Fig. 6. Depth dependence of saturated hydraulic conductivity K_s (left) and saturated water content θ_s (right).

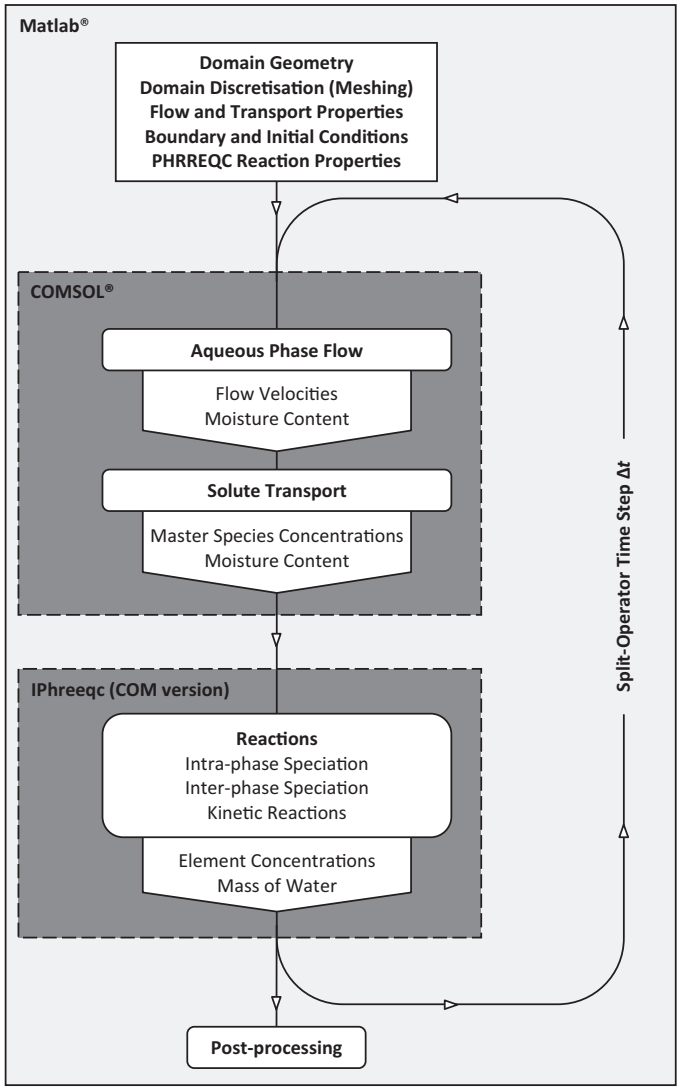

Fig. 7. Program flow and structure.

residue sand. The employed software results from coupling the multipurpose finite-element solver COMSOL [61] with a component object model (COM) version of IPhreeqc. IPhreeqc is a version of the geochemical modelling framework PHREEQC [29] that is specifically designed for coupling to multi-component solute transport simulators [62].

The main modules of the coupled software and their interactions are illustrated in Fig. 7. The coupling code is executed within the MATLAB scripting environment [63], which contains the split-operator procedure, manages data transfer between the modules and performs pre- and post-processing tasks. From MATLAB, the computation of aqueous phase flow and solute transport for a single time step is directed to the COMSOL module. After updated liquid phase saturations and solute concentrations are transferred back to the MATLAB workspace, the assembly of chemical components that constitutes the liquid phase is sent to IPhreeqc for geochemical speciation using its COM interface. The main advantage over existing couplings of flow and multispecies transport codes with PHREEQC as reaction engine, such as PHTRAN [64], PHT3D [65] and PHWAT [66], results from the fact that IPhreeqc saves in memory the entire geochemical system state between calls to it. Thus, only the information that is relevant to flow and transport computations (liquid phase saturation and element concentrations) needs to be extracted and transferred to COMSOL. In addition, the data transfer is processed entirely in memory, which avoids inefficient writing and reading of data files. A detailed presentation of the software is provided in [67]. Additional features that were specifically implemented for the presented simulations of bauxite residue sand are documented in the Appendices A–C.

5. Meteorological conditions

In the absence of vegetation, rainfall and evaporation are the driving forces of soil moisture movement and solute transport in the field. Thus, the geochemical evolution of residue sand, the volumes of drainage, and the magnitude of fertilizer leaching, strongly depend on the local meteorological conditions. Daily rainfall and pan evaporation were obtained from ALCOA's meteorological records for the Pinjarra residue storage area (latitude: −32.647036, longitude: 115.930309). Missing values in the evaporation time series were reconstructed by fitting the amplitude and phase of a sine function with wavelength of 365 d to the measured data. The dominance of seasonal fluctuations of evaporation was verified by means of Fourier analysis. Gaps in precipitation records were filled by linear interpolation between measurements. Mean annual precipitation after the reconstruction of missing data amounts to 1005 mm. This value agrees well with the 967 mm y^{-1} measured at the town of Pinjarra during the period 1877–1991 [68]. The mean annual value of reconstruction potential evaporation (2400 mm y^{-1}) is considerably higher than the value of 2075 mm y^{-1} from an independent 10-y record (1980–1990) [69]. Nevertheless, the interpolation method for potential evaporation was retained because the influence of evaporation on the overall water balance in the highly conductive sand is limited by water availability in the surface layer. The reconstructed time series of rainfall and potential evaporation at the Pinjarra residue storage site are illustrated in Fig. 8.

In its current form, the model represents bare residue sand prior to or shortly after plant seeding. Therefore, the influence of plants on water availability and water quality is not incorporated in the model. As shown in Wissmeier and Barry [67], however, element-specific root water uptake can be included into the model by using space- and pressure-dependent sink terms in solute transport equations.

6. Simulation of a field lysimeter

Currently, no data on fertilizer leaching in residue sand profiles under field conditions are available. At ALCOA's Pinjarra site, however, a field lysimeter has recently been constructed to quantify water and nutrients dynamics in rehabilitated residue sand [70]. In the following, we present a simulation of the geochemical evolution of fertigated and gypsum-amended residue sand in this field lysimeter in response to rainwater leaching under the prevailing meteorological conditions. The simulation period starts with the construction of the lysimeter in August 2007 and ends after 930 d in February 2010.

6.1. Domain, boundary and initial conditions

The lysimeter consists of a 3-m deep pit with vertical walls and a square surface area with sides of 24 m length. The pit is sealed with a high-density plastic liner and drained by regularly spaced (2.5 m spacing) drainage pipes located at 2.8 m below ground level. The domain was simulated as a 2D slice orthogonal to the drainage pipes. Due to symmetry planes halfway between the drainage pipes, at the midpoint of the drainage pipes and at the lateral boundaries, the domain could be reduced to a 1-m wide and 3-m deep column.

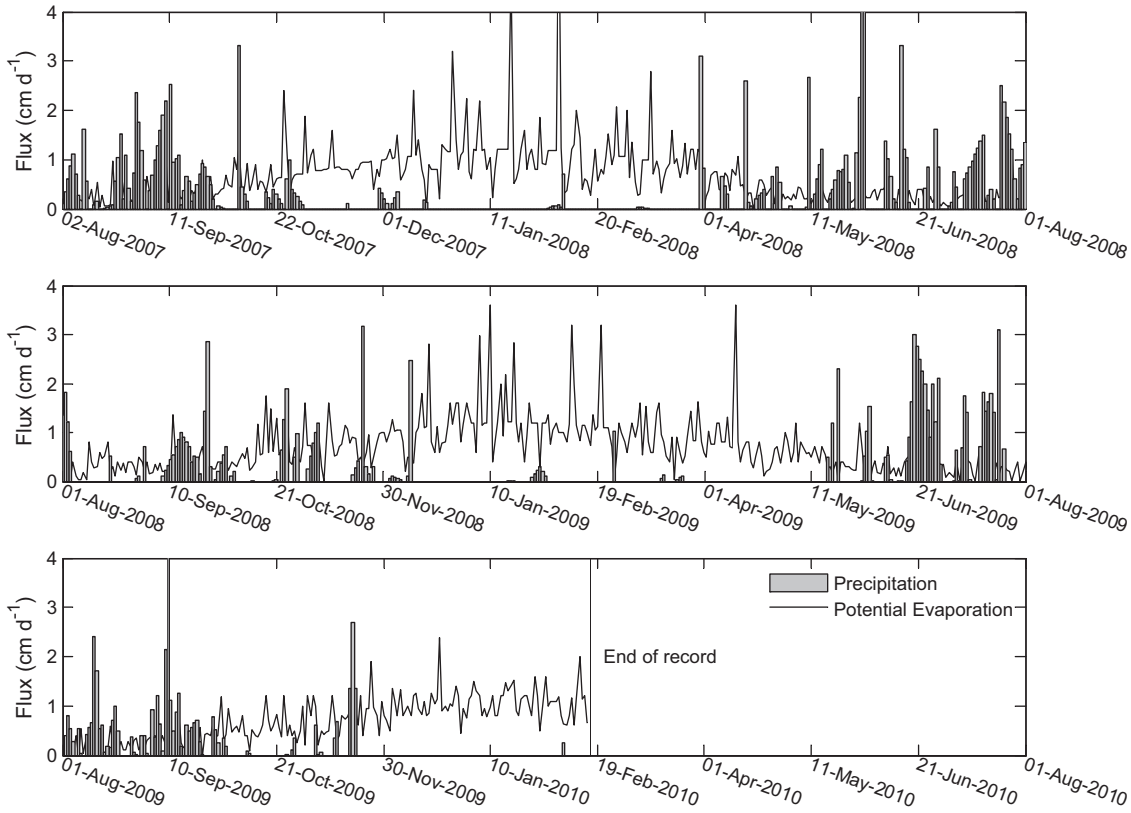

Fig. 8. Time series of rainfall and potential evaporation with reconstructed missing values.

The simulation domain and its finite-element discretization are displayed in Fig. 9. The half circle at $x = 0$ m, $z = -2.8$ m represents part of the drainage pipe where a seepage face boundary according to Eq. (C.1) in Appendix C with $k_{sp} = 10^{-4}$ s^{-1} was applied. At $z = 0$, an atmospheric boundary according to Eq. (C.4) with $H_{crit} = -30$ m, $\xi = 0.4$ s^{-1}, $H_{po} = 0$ m and $k_{po} = 10^{-4}$ s^{-1} was used. A zero-flux condition was employed for the remaining boundaries. The upper part of the domain with predominantly vertical flow was discretized by a quadrilateral mesh with a vertical element size of 3×10^{-3} m at the top boundary. The fine discretization was necessary to capture the sudden changes between infiltration and evaporation in the highly conductive sand. From $z = -2$ m downwards, a triangular mesh with a compressed z–direction and local refinement around the seepage boundary was used. The initial pressure head at the start of the simulation was taken as -1 m. At the top boundary, equilibrium of the infiltrating and evaporating rainwater with atmospheric CO_2 at 3.16×10^{-4} atm and O_2 at 1.99×10^{-1} atm was assumed. The split-operator time step for alternations between flow, transport and reaction calculations was set to 1 d.

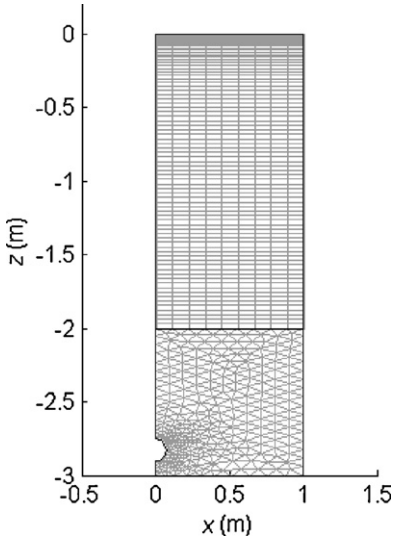

Fig. 9. Lysimeter simulation domain and finite-element representation.

6.2. Fertigation and gypsum amendment

Further to its natural geochemical properties, residue sand in the 0–1.5 m depth interval was amended with gypsum at a rate of 1% by weight. Furthermore, the top 0.2 m of the profile received a one-off addition of 2.7 t/ha of inorganic fertilizer mix mainly comprised of di-ammonium-phosphate (DAP), K_2SO_4 and $MgSO_4$. Phosphate (from DAP) in contact with gypsum is likely to reprecipitate as hydroxyapatite, which is why this mineral was included in the simulations with an initial amount of 0. This is also in agreement with observation in an independent column experiment (data not shown).

The amendments were included in the model through additional equilibrium dissolution reactions according to the reaction formulas, equilibrium constants and amounts listed in Table 4.

As can be seen from Eq. (1), the rate of concentration changes due to the kinetic dissolution of TCA and sodalite is dependent on the ratio of reactive surface to solution volume. In unsaturated residue sand with an average moisture content of 0.2, this ratio is approximately 40 times larger than in the acid neutralization experiment. Therefore, the assumption of local thermodynamic equilibrium was extended to TCA and sodalite.

Table 4
Fertilizer and amendment properties.

Mineral name reaction formula	Equilibrium constant	Relative amount (mol l_{soil}^{-1})
Gypsum[a] $CaSO_4{:}2H_2O = Ca^{+2} + SO_4^{-2} + 2\,H_2O$	$10^{-4.61}$ [c]	1.10×10^{-1}
DAP[b] $(NH_4)_2HPO_4 = 2\,NH_4^{+} + HPO_4^{-2}$	$10^{0.3}$ [d]	5.67×10^{-3}
Arcanite[b] $K_2SO_4 = SO_4^{-2} + 2\,K^{+}$	$10^{-1.776}$ [e]	2.41×10^{-3}
MgSO4[b] $MgSO_4 = Mg^{+2} + SO4^{-2}$	$10^{4.8781}$ [f]	1.50×10^{-4}
MnSO4[b] $MnSO_4 = Mn^{+2} + SO_4^{-2}$	$10^{2.669}$ [c]	1.42×10^{-4}
CuSO4[b] $CuSO_4 = Cu^{+2} + SO_4^{-2}$	$10^{3.01}$ [c]	1.55×10^{-4}
Zincosite[b] $ZnSO_4 = Zn^{+2} + SO_4^{-2}$	$10^{3.01}$ [c]	1.11×10^{-3}
Borax[b] $Na_2(B_4O_5(OH)_4){:}8H_2O + 2\,H^{+} = 4\,B(OH)_3 + 2\,Na^{+} + 5\,H_2O$	$10^{12.464}$ [e]	2.62×10^{-5}
Hydroxyapatite $Ca_5(PO_4)_3OH + 4\,H^{+} = H_2O + 3\,HPO_4^{-2} + 5\,Ca^{+2}$	$10^{-3.421}$ [g]	0.00

[a] Applied to the top 1.5 m.
[b] Applied to the top 0.2 m.
[c] minteq.dat.
[d] Calculated from solubility in pure water [71].
[e] pfitzer.dat.
[f] llnl.dat.
[g] phreeqc.dat.

6.3. Results and discussion

6.3.1. Dynamic water balance

Results of the dynamic water balance for the simulation period of 930 d starting on 1 August 2007 are displayed in Fig. 10. The surface flux in (Fig. 10a) was normalized by the infiltrating area and reflects the strong events during winter, which were immediately followed by marked evaporation. Despite high potential evaporation during summer, actual evaporation was effectively shut down due to the limited water availability in the upper soil profile. Discharge in Fig. 10b was also normalized with respect to the infiltrating area for better comparability. The water infiltrated during the 2007 rainfall season at the beginning of the simulation reaches the drainage pipe after 60 d. Before any discharge is produced, the domain below the drainage pipe was saturated. The initial filling of the lysimeter bottom during the first 60 d can be followed in the evolution of average moisture contents (Fig. 10c). The fast discharge recession leads to very low outflow rates during summer months. Despite the fully saturated lysimeter bottom, the moisture content frequently declined below a domain average of 0.15 during summers. This is also confirmed experimentally by in situ moisture probes and neutron probe measurements.

Overall, the simulation of soil moisture in the lysimeter (Fig. 10) indicates very dry conditions throughout the entire simulation period. During summers, the water content frequently decreased to values close to the residual (i.e., plant-unavailable) moisture content in the upper metre of the profile. Despite low moisture contents, the average fluid pressure did not drop below the permanent wilting point (PWP: $h = -15$ bar). However, near the surface the PWP was frequently reached. In addition, the sand contains only marginally more water at -1 bar than at -15 m due to the steep gradient of water retention $dh/d\theta$ (Fig. 5). Even during rainfall seasons, the moisture content hardly exceeded 0.2 in the upper 2.5 m of the domain. Despite the poor water holding capacity of the sand, only about 46% of the total rainfall left the lysimeter as drainage. The rest was lost by evaporation or stored in the initially dry profile. Thus, the water supply alone imposed conditions that were challenging, but not inhibiting, for plant growth in the lysimeter.

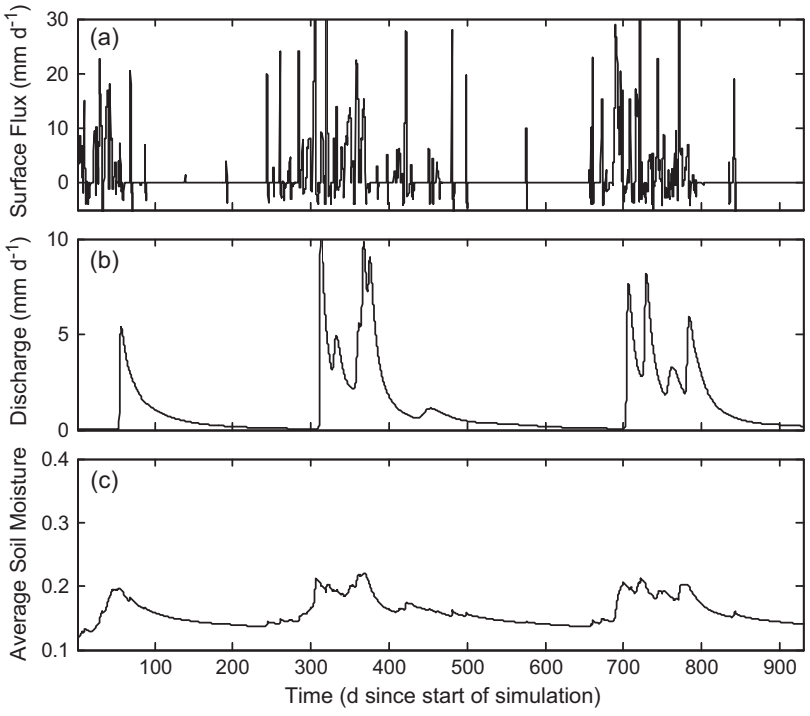

Fig. 10. Dynamic water balance of lysimeter simulation with (a) surface flux (mm d^{-1}), (b) drainage at the drainage pipe (mm d^{-1}) and (c) average soil moisture content θ.

6.3.2. Solution chemistry

Fig. 11 illustrates the evolution of vertical profiles of moisture content, pH and selected solution element concentrations at the right domain boundary ($x = 1$ m). Despite the local outflow at the drainage pipe ($x = 0$ m), only minor lateral variations of geochemistry and moisture conditions were observed. Moisture content profiles show the development of the groundwater table below the drainage pipe as response to the winter rainfall around 50 d. The upper part of the soil column then dried out over summer until the beginning of the following rainy season. The pH profiles show a fast reduction of pH in the upper soil profile to about 11 from an initial value of 12.5 caused by gypsum dissolution and calcite precipitation. In the lower profile below −1.5 m, the pH was governed by dissolved natron.

With the second winter's rainfall starting at around 300 d, the pH reduced to values around 10 in the upper soil profile and with the third winter's rainfall in the entire profile. The initially high Na concentration from natron dissolution was flushed into the lower part of the domain with the first rainfall. The second rainfall period almost completely removed Na from the system, due to the comparatively low solubility of sodalite and analcime. Carbon, as carbonate (CO_3^{-2}) from natron dissolution, immediately reprecipitated as calcite in the upper part of the domain due to the large supply of Ca from gypsum dissolution. The remaining carbon in the un-amended region of the domain was removed after approximately 50 d. Ca concentrations show a complex pattern mainly governed by the solubility of calcite and gypsum, both of which are controlled by pH. The decrease in Ca at the top boundary during the second and third rainfall period indicates complete removal of gypsum, which was not observed in the field. This is most likely due to non-equilibrium of gypsum with the soil solution as result of inhomogeneous amendment of the gypsum. During the following evaporation events, the upward flowing solution was concentrated due to the removal of H_2O at the surface. However, evaporation essentially stops during the dry season because of low moisture contents at the surface. Sulphur, as sulphate (SO_4^{-2}) behaved similarly to Na in the region of gypsum amendment above −1.5 m. Its high initial concentration, resulting from the equilibrium between gypsum and calcite, was flushed almost entirely within the first 300 d. Nitrogen (N(−3) as sum of NH_4^+ and NH_3) was decoupled from oxidized forms (e.g., NO_3^-) to avoid instantaneous conversion to N(+5). N(−3) concentrations are displayed representative for the fertilizer elements copper (Cu), zinc (Zn) and boron (B), which show very similar concentration patterns. Their concentration ranges correspond to the amounts of the applied fertilizer minerals (Table 4). The fertilizer elements were carried downwards through the soil profile with the first winter rainfall, and with the second winter's rainfall, they were flushed from the profile without significant retention. Due to high Ca concentrations the model predicted reprecipitation of hydroxyapatite ($Ca_5(PO_4)_3OH$), which retains phosphate (P) in the profile. K concentrations were significantly retarded compared to nitrogen because of temporary adsorption on the cation exchange sites. Magnesium (Mg) shows a mixture of the conservative transport pattern of nitrogen and the exchange pattern of K. High initial Al concentrations in the lower half of the domain resulted from the dissolution of TCA, which is enhanced by reprecipitation of Ca as calcite. In the gypsum-amended part of the soil, TCA dissolution was inhibited by gypsum dissolution. Silica (Si) shows the same concentration pattern as chloride. Both elements were controlled by the dissolu-

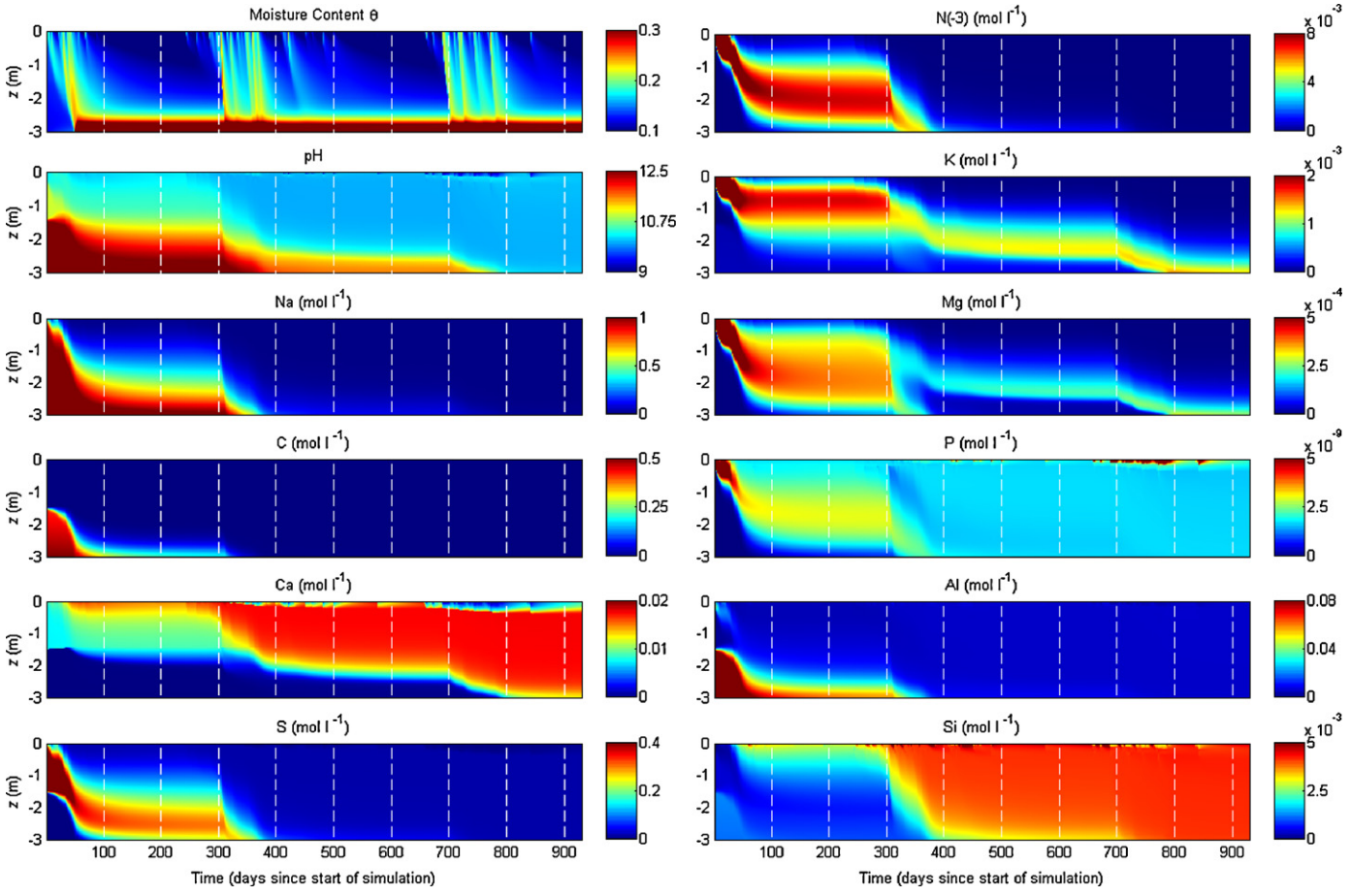

Fig. 11. Evolution of moisture content, pH and concentration of selected elements at the right domain boundary of the lysimeter simulation.

tion of sodalite, which was activated after the complete removal of TCA.

6.3.3. Minerals

Fig. 12 illustrates the evolution of the main mineral phases in residue sand. Muscovite and analcime did not show any significant response towards leaching during the simulation period and so are omitted in the figure. The other residue minerals show only minor changes in the upper few decimetres of the domain. Gypsum was removed from the top 0.5 m after 3 y of rainfall. However, due to the equilibrium assumption, a considerable amount of gypsum in the top 1.5 m instantaneously transformed into calcite, taking up most of the CO_3^{-2} from natron dissolution. Apart from this increase, calcite shows little response to leaching. Almost half of the initial amount of TCA was immediately dissolved in the untreated residue sand where Ca re-precipitated to calcite with the CO_3^{-2} from natron dissolution. This transformation was suppressed by gypsum in the in the upper part of the domain. However, the fertilizers in the top 0.2 m enhanced TCA dissolution. Leaching of the third rainfall season around 700 d removed TCA from the top 0.2 m. Sodalite shows no reaction towards gypsum and fertilizer amendment. It was slowly leached from the first few centimetres of the soil profile during the three simulated rain seasons once TCA and gypsum were removed.

6.3.4. Cation exchange

The evolution of the exchange species is illustrated in Fig. 13. The initial exchanger composition was dominated by Na, which was replaced mainly by Ca during the course of the simulation. Al is omitted in the figure due to insignificant adsorption in the high pH environment, where it was mainly present in anionic form as $Al(OH)_4^-$. At the transition from the Na to Ca-dominated exchanger, adsorption of K, N(−3), Mg and Mn took place. Despite the higher affinity of standard exchangers for divalent ions, K was the most adsorbed fertilizer element. This is because of its higher concentration compared to divalent fertilizer elements and its large affinity relative to other monovalent fertilizer elements. N(−3) as NH_4^+, which was retained in the upper part of the profile during the first summer, was almost completely removed during the second rainfall period. The low adsorption of N(−3) resulted from its speciation into uncharged NH_3 at pH values above 9. The amount of adsorbed Mg, which is representative for the adsorption pattern of Mn (maximum adsorbed amount 1.5×10^{-5} mol l_{soil}^{-1}), increased after 400 d. The adsorption of zinc and copper was insignificant due to low solution concentrations (maximum adsorbed amounts 10^{-8} mol l_{soil}^{-1} and 3×10^{-11} mol l_{soil}^{-1}, respectively).

Overall, the predicted geochemical conditions in the lysimeter were still unfavourable for plant growth after 3 y, both in terms of water availability and quality. Even though the main soluble ions Na^+ and SO_4^{-2} were flushed from the system, a pH of 10 was maintained. The plant nutrient status was not sustainably improved by fertilizer amendment. Only K was significantly retained by initially Na-filled adsorption sites. Adsorption of other fertilizer cations including NH_4^+ was insignificant due to (i) their low concentrations compared to the major solutions ions Na and Ca, (ii) their speciation into neutral or negatively charged ions at high pH, and (iii) the low exchange capacity of residue sand. The chromatographic sequence from a Na-dominated exchanger through the temporary adsorption of fertilizer cations to a Ca-dominated system can be interpreted as a snowplough [72–74]. The buffering minerals, TCA, sodalite and calcite that stabilize the pH around 10 were removed from the top few centimetres of the profile. As intended by the gypsum

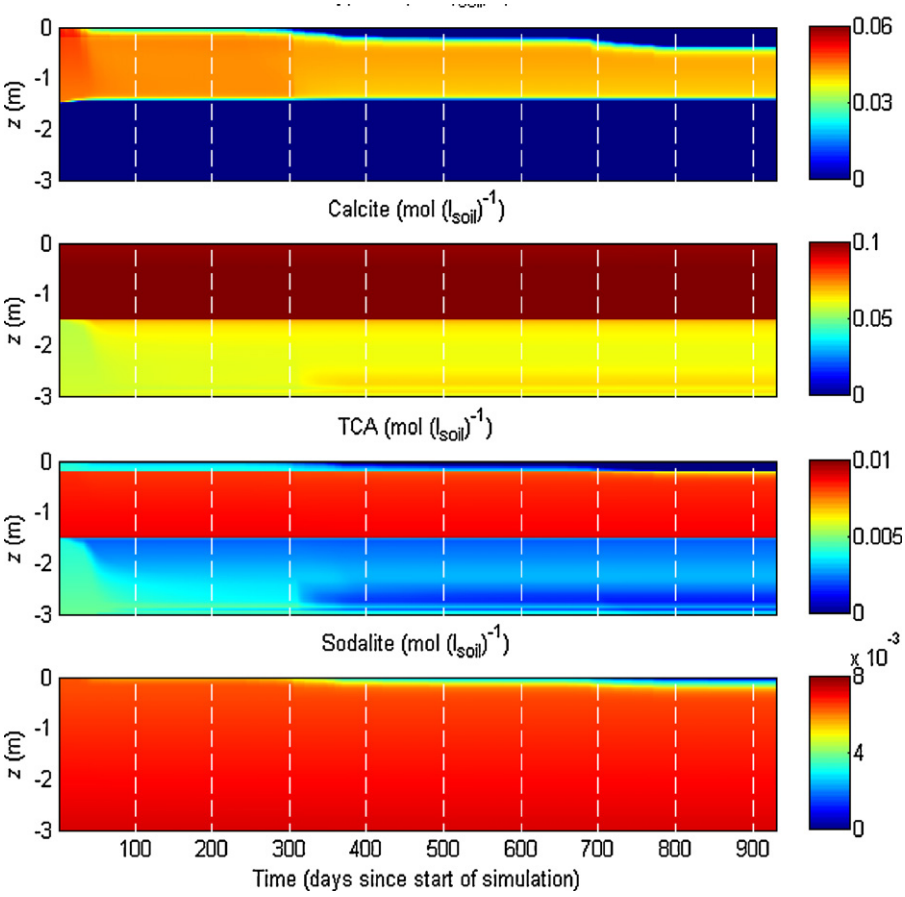

Fig. 12. Evolution of the main minerals at the right domain boundary of the lysimeter simulation.

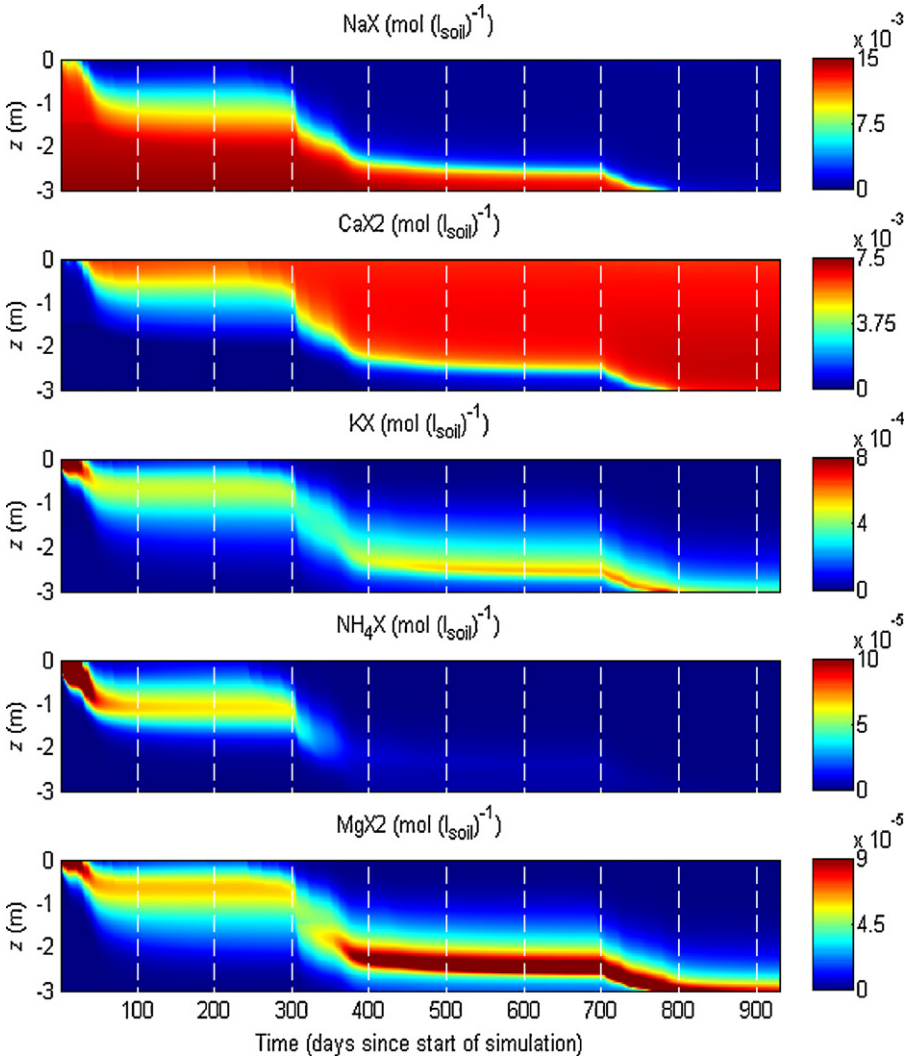

Fig. 13. Evolution of the exchanger composition at the right domain boundary of the lysimeter simulation.

amendment, solution alkalinity was converted to calcite [75,76]. This procedure, however, did not remove the alkalinity from the system converted it into solid form and prevents the removal of TCA [77].

7. Simulation of surface cover for storage facilities

In order to evaluate the performance of fertigated and gypsum-amended residue sand as a surface cover for storage facilities, the hydrogeochemical model was applied to a stratum of sand overlaying low permeability residue mud. Apart from the domain geometry and discretization, the hydrological and geochemical conditions of the lysimeter simulation were adopted including fertigation and gypsum amendment. In contrast to the lysimeter with predominantly vertical flow, the development of a water table at the border to the residue mud introduces a considerable horizontal flow component.

7.1. Domain, boundary and initial conditions

The simulation represents a 3-m thick by 100-m wide layer of residue sand on top of a storage impoundment. Due to symmetry across the centre line, the actual simulation domain was confined to a slice of the cover layer from $x = 0$ m to $x = 50$ m with a symmetry boundary at the right hand side border of the domain. The domain was represented by 10,829 computational nodes. For enhanced lateral drainage, the cover layer was conceptualized with a slope of 1.74%. Water losses at the interface to the residue mud at the domain bottom were approximated by a constant flux of 8.3×10^{-7} m s^{-1} in water-saturated conditions and zero flux otherwise. The magnitude of this deep percolation was taken as the saturated hydraulic conductivity of red mud [3], in which case the flux corresponds to gravity-driven drainage. The left hand side of the domain was represented by a seepage face boundary according to Eq. (C.1) with a stiff-spring constant of $k_{sp} = 10^{-3}$ s^{-1}. Atmospheric forcing of the system was imposed via an atmospheric boundary condition at the top of the domain. In order to predict the evolution of the sand cover for 5 y, the measured meteorological time series of 3 y were repeatedly applied to the soil surface.

7.2. Results and discussion

7.2.1. Dynamic water balance

The dynamic water balance of the surface cover simulation is illustrated in Fig. 14. For better comparability with the lysimeter simulation (Fig. 10), the y-axis scaling was retained. Compared to the lysimeter simulation the surface cover exhibits much larger water storage capacity and slower recession of discharge during dry periods due to impeded drainage (Fig. 14b). As in Fig. 10, the

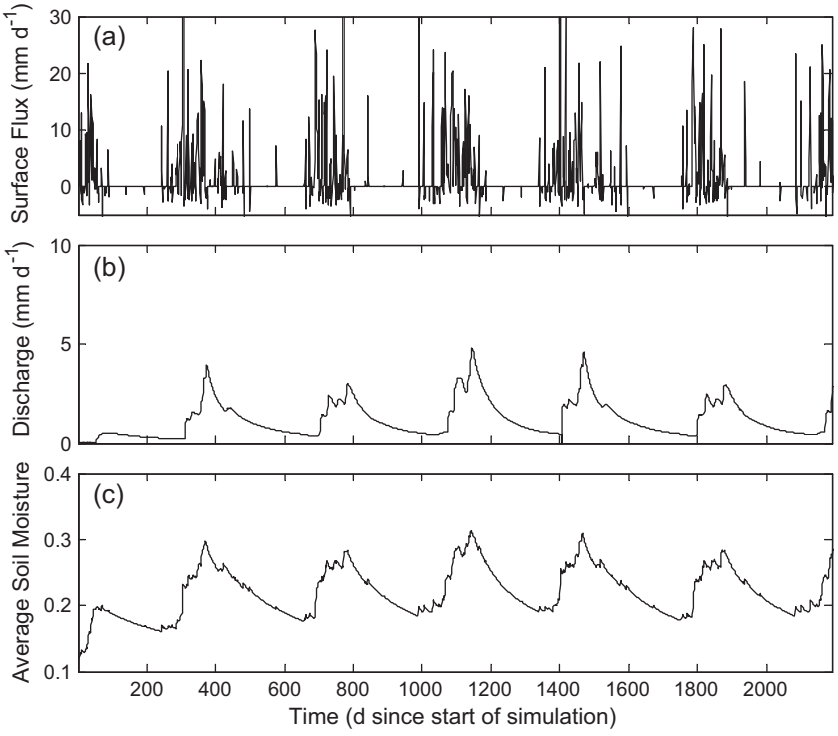

Fig. 14. Dynamic water balance of surface cover simulation, with (a) surface flux (mm d^{-1}), (b) drainage (mm d^{-1}) and (c) average soil moisture content θ.

drainage flux was normalized to the inflow area for comparability. At the beginning of the simulation period, a perched water table evolved at the border to the low-permeability mud. Due to this water table, the average soil moisture (Fig. 14c) was at much higher levels (0.2–0.3) compared to the lysimeter simulation.

7.2.2. Solution chemistry

Time-dependent profiles of normalized soil moisture, $\Theta = \theta\text{-}\theta_r/\theta_s\text{-}\theta_r$, selected total element concentrations and pH are displayed in Fig. 15 with different scales for the *x*- and *y*-axes. Different colour scales were used for the plots from 1 to 50 d and from 400 to 1825 d because the low fertilizer concentrations after the first rainfall period would otherwise be indistinguishable in the later profiles. Display times were selected during the first rainfall period (1–50 d), in the middle of the second rainfall period (400 d), after the third rainfall period (1000 d) and at the end of 5 y of atmospheric leaching (1825 d).

Normalized water contents illustrate the build-up of soil moisture at the border of the residue mud and the evolution of a perched water table. The results at 400 and 1000 d show water table fluctuations from winter to summer.

Until the last profile at 1825 d, Ca that mainly originates from gypsum and TCA dissolution did not enter the saturated zone. Declining concentrations at the top of the domain indicate complete removal of gypsum and TCA. Na was flushed from the unsaturated zone with the first rainfall event. Due to the velocity field in the saturated groundwater lens, concentrations were more persistent towards the right hand side of the domain. However, after the third rainfall season (1000 d) most of the Na has been removed. N(−3) is representative for all fertilizer elements besides K. Through dilution and dispersion, concentrations decreased with the first infiltration water. During the second rainfall period around 400 d, the fertilizers were removed from the unsaturated zone. However, they remained in the groundwater lens at roughly a tenth of their original concentration. Fertilizer concentrations decreased further during the third rainfall season until they were removed completely after 5 y of leaching. The behaviour of K, the most adsorbing element, was very similar to N(−3). As result of the exchange process, however, its removal was delayed compared to the other fertilizer elements. During the first rainfall period, the pH behaved similarly to the lysimeter simulation because of essentially 1D flow. After the perched water table has established, two pH regions were separated by the line of the groundwater table in moist conditions. The pH in the saturated region was persistent until it was eventually leached to pore water levels in the unsaturated zone after 5 y. In the profiles at 1000 and 1825 d the removal of gypsum and TCA at the top of the domain decreased the pH to around 9.

7.2.3. Minerals

The evolution of the main minerals in the surface cover is illustrated in Fig. 16. During 5 y of rainfall, gypsum was removed from the top metre of the profile. In this zone, calcite showed hardly any response to leaching. However, additional precipitation was predicted at the lower boundary of the gypsum-amended region and in the saturated zone. TCA was removed from the top 0.5 m and from the saturated zone, while sodalite was only removed from the top few decimetres. Exchange processes are dominated by Na–Ca exchange, and are omitted since the results are similar to those for the lysimeter.

In summary, the results show that water availability was improved in the surface cover by the formation of a perched groundwater table. Waterlogged conditions with evaporation-induced salt accumulation at the soil surface [78–80] were avoided by the slope of the underlying low-permeability mud and lateral drainage. Due to its large water volume, the saturated zone acted as a buffer for infiltrating solutes and retained fertilizer ions. However, enhanced water retention also retained adverse soil properties such as high pH and Na concentrations, which decreased the efficiency of natural leaching.

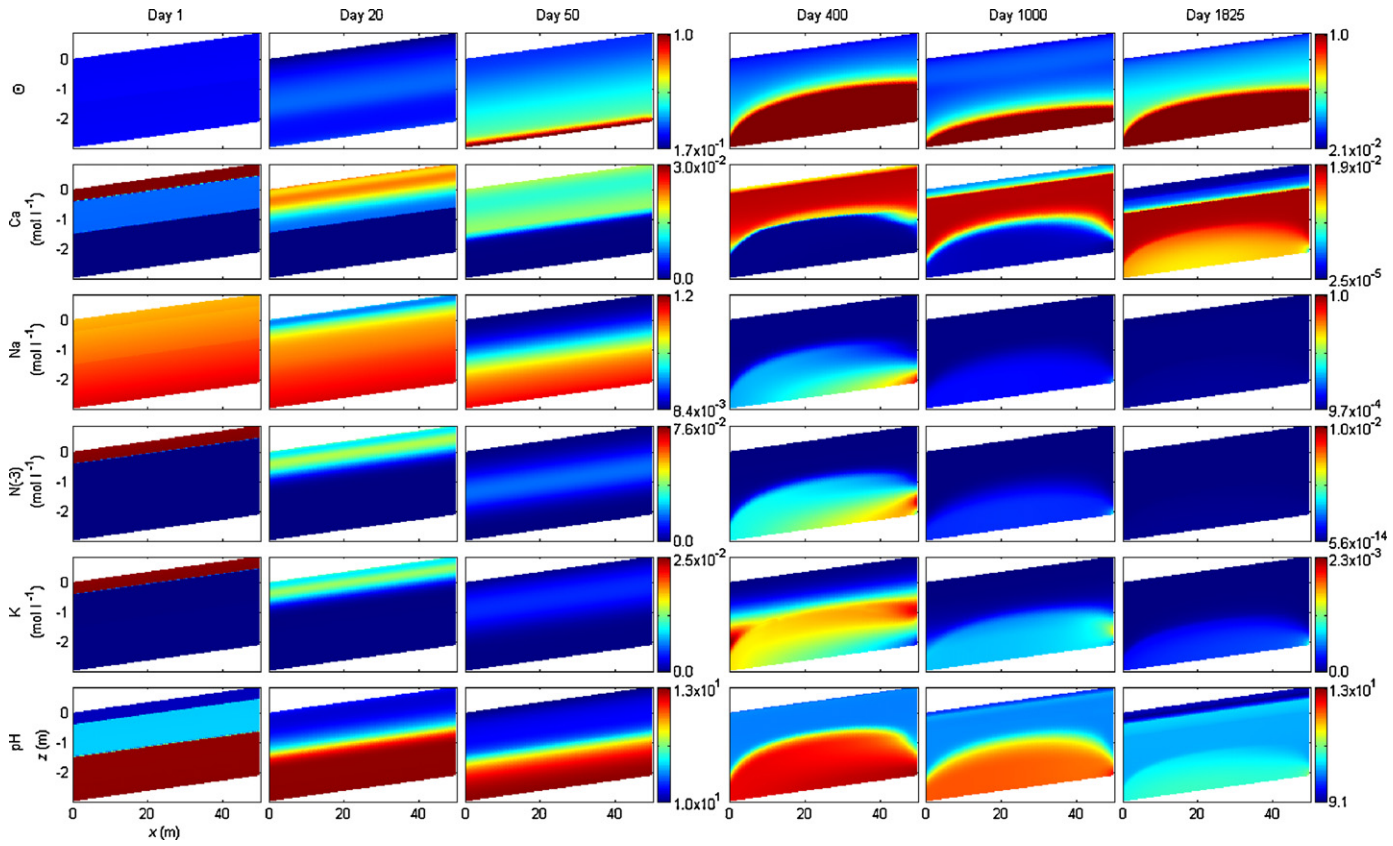

Fig. 15. Evolution of normalized moisture content, concentrations of selected elements and pH profiles of the surface cover simulation at 1, 20, 50, 400, 600 and 1825 d.

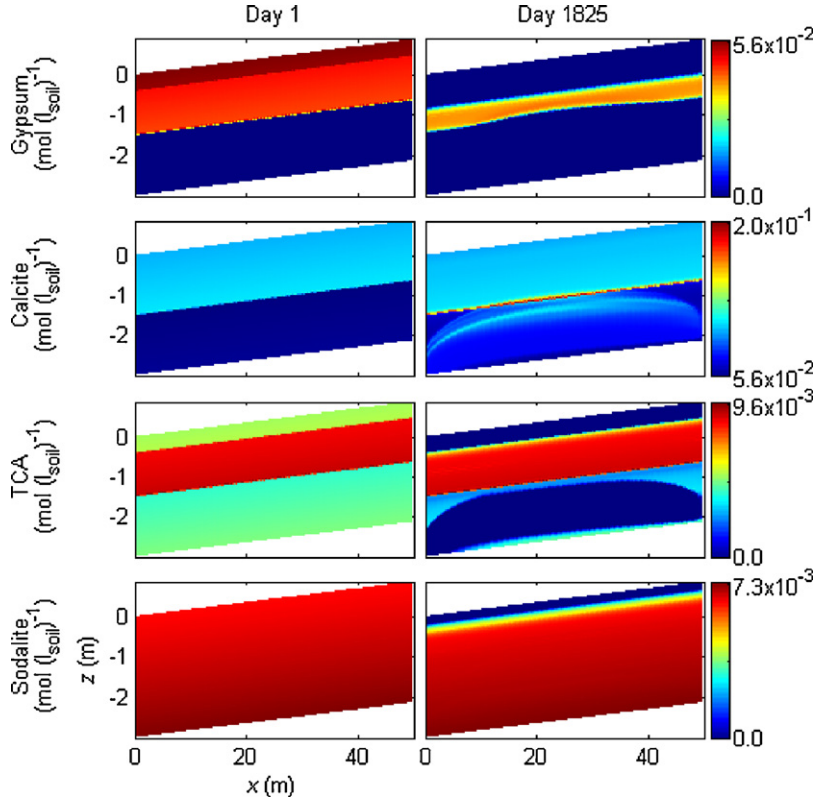

Fig. 16. Evolution of the main minerals of the surface cover simulation for 1 and 1825 d.

8. General discussion

8.1. Model uncertainties

The model for mineral reactions in bauxite residue sand comprises large uncertainties, even though all components of the mineral assembly have been previously identified in residue of different origins [30,34,41,81]. The mineral assembly as deduced from acid neutralization alone is not unique and other combinations of minerals may reproduce pH buffering equally well. Sodalite and additional amounts of natron, for instance, yield excellent agreement with acid neutralization at 96 h. However, this would require the kinetic dissolution of natron at a timescale of days, which is not plausible unless it is partially occluded within the profile. In order to increase the reliability of the predictions, detailed quantification of the reactive minerals specifically for Pinjarra residue sand would be required. Furthermore, equilibrium constants vary widely among authors and databases, particularly for different forms of tricalcium aluminates but also for muscovite and analcime. Measurements of the stoichiometry and solubility of reactive minerals on phases isolated from the residue would be desirable. This is also important because most reactive minerals form during the refining process, so that their reactivity and stoichiometry depends on the bauxite source and processing conditions [32,33,39,82,83]. The fact that Khaitan et al. [34] attribute the pH buffering capacity of residue from Jamaican bauxite mainly to TCA and calcite whereas Menzies et al. [41] and Snars and Gilkes [30] hold mainly sodalite and calcite responsible for pH control indicates the large uncertainty in the recent literature. In the mineral assembly determined in this study, both phases contribute to pH buffering in roughly equal parts. Acknowledging the large uncertainties, the derived mineral composition can be regarded as a surrogate for major geochemical properties such as pH, electrical conductivity and Na concentrations. Concentrations of elements that are not components of an included mineral, such as iron, Mg and titanium (Ti), cannot be predicted.

In a recent study, Phillips and Chen [14] found a large contribution (8–12 cmol kg_{solid}^{-1}) of pH-dependent variable charge adsorption sites to the overall adsorption characteristics of residue sand. Menzies et al. [41] measured the effective exchange capacity of seawater neutralized residue sand as 18.6 cmol kg_{solid}^{-1} from which they attributed 6 cmol kg_{solid}^{-1} to variable charge. These values exceed the cation exchange capacity measured in this study by a factor of 10–20. However, both previous studies rely on compulsive exchange of K^+ with NH_4^+. As shown in Fig. 4b, considerable amounts of K are released by mineral dissolution. Therefore, K concentrations cannot be considered to result solely from exchange processes, which may lead to an overestimation of the effective exchange capacity. The presumed pH-dependency of the exchange sites may in fact reflect the solubility of the source mineral (e.g., muscovite). On the other hand, the effective exchange capacity in our study may have been reduced by the washing procedure, particularly through the removal of surface aluminous and ferric oxides that contribute to variable charge adsorption sites. Nevertheless, we employ the lower value of cation exchange capacity on washed residue since it gives a more conservative estimate of nutrient retention. Because pH levels during the simulations were well above the point of zero charge of ferrous and aluminous oxides [84,85], charge characteristics are not expected to change significantly. This justifies the use of a simple exchange model for adsorption. However, the adsorption behaviour of cations onto zeolites such as sodalite is influenced by the window size of their cage structure [86–90]. Thus, the applicability of standard affinity constants for the simulation of cation exchange remains uncertain [91].

The dynamic water balance is regarded as relatively reliable since the parameters for soil moisture movement are directly measured or derived from measurements according to standard procedures (e.g., water retention).

An obvious weakness of the simulations is the lack of in-depth model validation due to the scarcity of analytical data.

8.2. Implications for bauxite residue management

Despite the model uncertainties, the main results are plausible and consistent with observations. Because the model is adapted to the geochemical and meteorological conditions at the Pinjarra refinery, findings are site-specific but can be generalized to residue sand with similar properties and in comparable climatic conditions.

The lysimeter simulation illustrates the poor water retention in the residue sand with low plant-available soil moisture content. Thus in well-drained systems water availability is a limiting factor for plant growth. The simulation of the cover layer shows that the moisture status in residue sand can be improved by the appropriate design of the horizontal distance between drains, the thickness of the cover layer and its slope. If these parameters are not chosen carefully, for example if the distance between drains is too large, waterlogged conditions with adverse effects on plant growth may result (simulation results not shown). The development of a shallow water table increases evaporation losses during the summer months. Although not observed in our simulations, this may lead to salt accumulation at the soil surface [78,79]. The amendment of residue sand with fine-textured residue mud would improve the soil water retention but at the same time worsens the geochemical properties through enhanced pH buffering [92]. Compared to the hydrological situation, the geochemical properties of the residue sand are seen as more severe constraints for plant growth. Mineral reactions in amended fresh residue sand are governed by the initial dissolution of natron and gypsum, where Ca and CO_3^{-2} precipitate as calcite while the soluble $Na_2SO_4^{-2}$ is flushed. Even though gypsum amendment reduces the solution pH to 10, leaching of TCA and therefore the sustainable decrease of pH buffering in the sand is inhibited. From the main buffering minerals, TCA and sodalite are very resistant to rainwater leaching due to their low solubility. Efficient retention of fertilizers is prevented by (i) the low cation exchange capacity of residue sand, (ii) competition with high levels of Ca and Na for exchange sites, and (iii) the speciation of fertilizer elements into uncharged or negative ions at elevated pH (e.g., NH_3). Therefore, the addition of fertilizers to gypsum-amended fresh residue sand only temporarily improves the plant nutrient status. Natural attenuation of gypsum-amended and fertigated residue sand through atmospheric leaching is not a viable long-term option to improve the hydrogeochemical properties for establishing a sustainable vegetation cover.

Instead, we propose a comprehensive treatment scheme that aims at improving all major aspects of soil fertility:

1. Removal of most soluble mineral fractions – e.g., through seawater neutralization [5,41,93,94] – to decrease the solid pH buffering capacity and attenuate the competition with fertilizer ions for exchange sites;
2. Amendment with a fine textured mineral soil (not residue mud) to improve water retention and cation exchange capacity;
3. Adaption of surface cover dimensions to the hydraulic properties of the substrate with regularly spaced drains to improve the water balance;
4. Amendment with organic fertilizer to establish a natural microbial community, increase the adsorption capacity [6,8,95–97]; and
5. Application of inorganic fertilizers [10,12,16,17,95,98] to improve the plant nutrient status.

9. Conclusions

We present the application of a software coupling of COMSOL and IPhreeqc for interactions of comprehensive geochemical reactions and 2D variably saturated soil moisture movement to evaluate the environmental behaviour of bauxite refining residue sand. The main findings of the simulations are:

- In well-drained residue sand, the average moisture content drops below 0.1 for extended periods during summer, which poses limitations to plant growth.
- By adapting the dimensions and drainage of residue storage facilities to the hydraulic properties of the cover material (e.g., mixtures of sand and clay), a plant-suitable moisture content can be maintained also during the dry summer months.
- Non-recurring fertilizer application on fresh residue sand does not alter the long-term plant nutrient status due to low cation exchange capacity, competition with predominant solution ions and speciation into neutral or negative form.
- Gypsum amendment ameliorates the pH to around 10 but suppresses the dissolution of TCA and therefore hampers the sustainable leaching of solid alkalinity.

Thus, we conclude that gypsum amendment and application of inorganic fertilizers alone does not sufficiently improve the geochemical conditions in residue sand to promote a vigorous and sustainable vegetation cover. Since the minerals in residue sand have a very high buffering capacity and annual recharge rates in southwest Western Australia are low, natural attenuation of the sand's pH via rainfall leaching is predicted to be in the order of tens of years. For the successful revegetation of residue storage facilities all aspects of soil fertility need to be addressed before residue sand can serve as valuable medium for plant growth. A logical step for future model development would be the incorporation of biological transformations by plants and soil microbes.

Acknowledgments

The authors acknowledge Chanelle Carter, whose contributions benefitting this study were sadly cut short by her untimely death. Partial financial support was provided by ALCOA World Alumina Australia, Pty. Ltd.

Appendix A. Sequential solution of flow and transport

Using the coupling of COMSOL and IPhreeqc, the simultaneous solution of the non-linear partial differential equation of variably saturated flow together with numerous transport equations for multi-component solutions in complex domains quickly becomes unstable with excessive memory requirements. In order to increase the efficiency and stability of COMSOL computations, flow and transport were solved sequentially using COMSOL's segregated solver. This assumes a strict one-way coupling between the two processes. Thus, the iterative solution of Richards' equation is only computed for the pressure variable. The resulting time-dependent flow field is then input into the multi-component solute transport equations, which are linear and thus easier and faster to solve.

Appendix B. Parallelization

During reaction calculations in IPhreeqc, each node of the discretized simulation domain is represented by an independent geochemical batch system. Thus, large domains require the computation of several thousands of batch systems, which may lead to long computation times particularly if complex kinetic reactions are involved. For increased computational efficiency, reaction calculations were parallelized, making use of MATLAB's *single program multiple data* algorithm. In this procedure, an IPhreeqc COM-object is initialized on each of the engaged processors and the number of batch systems for evaluation is distributed evenly. The speed increase that results from distributed reaction calculations scales well with the number of available processors.

Appendix C. Implementation of atmospheric and seepage face boundaries

The interface for Richards' equation in COMSOL's Earth Science Module provides predefined settings for pressure head and flux boundary conditions. In the case of seepage face and atmospheric boundaries, however, a flux condition may turn locally into a head condition and vice versa according to a head-based criterion [99,100]. Since the type of boundary condition cannot be changed during a simulation, the stiff-spring approach, where a Neumann statement about flux is used to achieve a Dirichlet condition for the pressure head, has to be employed [101].

A seepage face boundary conceptualizes a porous medium that drains freely and where the out-flowing water is removed rapidly enough such that it does not build up on the surface. Consequently, a zero head condition applies as long as there is potential outflow from the domain (the pressure head within the domain is greater than zero). In unsaturated conditions (negative pressure head), the boundary turns into a no-flow boundary. The stiff-spring representation of a seepage face boundary is given by

$$q_0 = \begin{cases} 0, & H_0 \le 0 \\ -k_{sp} H_0, & H_0 > 0, \end{cases} \tag{C.1}$$

where q_0 ($\mathrm{m\,s^{-1}}$) is the inward flux crossing the boundary, H_0 (m) is the actual pressure head at the boundary and k_{sp} ($\mathrm{s^{-1}}$) is the positive spring constant. The flux $-k_{sp}H_0$ must be of a magnitude sufficient to prevent build-up of water and fix the pressure head at the boundary effectively to zero. Therefore, the accuracy of the stiff-spring representation increases with the magnitude of k_{sp}, however at the cost of numerical efficiency and stability [102,103]. Atmospheric boundary conditions are governed by the recharge flux $r(t)$ ($\mathrm{m\,s^{-1}}$), which is the difference between the absolute values of rainfall and potential evaporation. In the case of bare soil evaporation, $r(t)$ is limited by the water availability in the soil. Once a critical negative pressure head, H_{crit} (m), at the soil surface is reached, the boundary conceptually switches from a specified flux boundary to a head condition. H_{crit} is the pressure potential of the atmosphere and a measure of the atmospheric evaporation demand [100]. In dry and hot weather situations, it may exceed in magnitude -10^3 m. Thus, in contrast to the seepage face boundary, the change between constant head and specified flux occurs in the dry range of the moisture spectrum, where H_0 is extremely sensitive to the applied flux. In order to avoid oscillations of the numerical scheme a smooth spring function is required that merges seamlessly with the flux in unconstrained conditions. For the representation of evaporation boundaries, we therefore make use of the following condition:

$$q_0 = -r(t)\tanh\left[\frac{\xi}{r(t)}(H_0 - H_{\mathrm{crit}})\right], \tag{C.2}$$

where ξ ($\mathrm{T^{-1}}$) is the derivative of q_0 with respect to H at H_{crit}, which determines implicitly the width of the transition zone between unconstrained and limited evaporation.

The behaviour of q_0 in the vicinity of H_{crit} is illustrated in Fig. 17. As H_0 approaches H_{crit}, the magnitude of the evaporation flux is reduced continuously until evaporation stops completely and even gives positive values (condensation) if H_{crit} is surpassed. This behaviour is consistent with the physical process, where evapo-

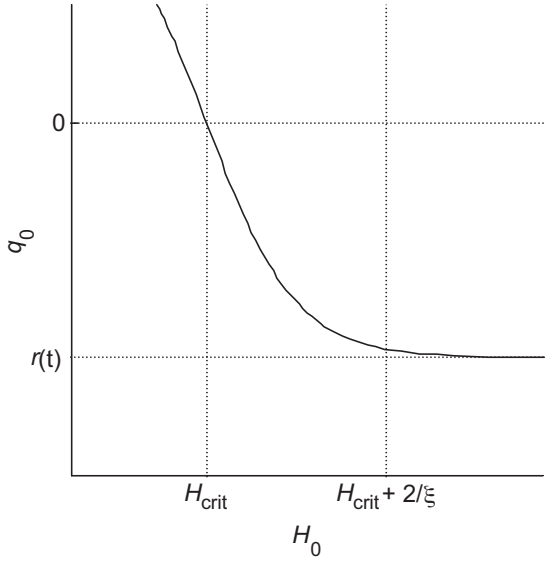

Fig. 17. Boundary flux during negative recharge in the vicinity of the critical pressure head H_a.

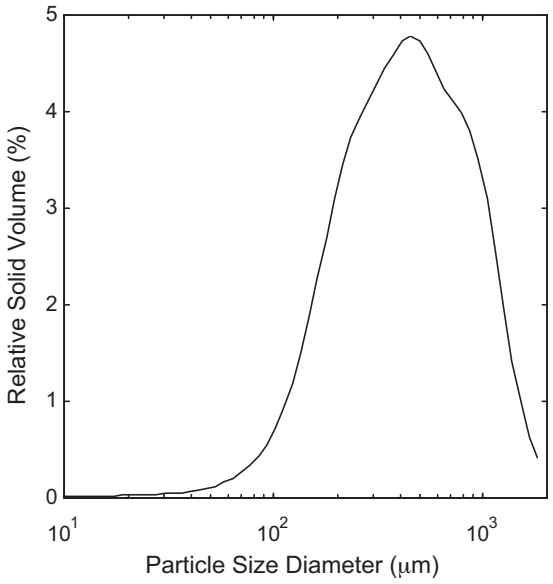

Fig. 18. Particle size distribution of washed residue sand.

ration from dry soils is gradually reduced due to limited water availability. Low values of H_{crit} require a larger smoothing zone (lower ξ) and very fine domain discretization near the boundary [104] in order to achieve numerical convergence.

In the case of positive recharge the boundary flux is limited by the infiltration capacity at the maximum surface pressure head H_{po} (m), which represents the maximum height of ponded water [56]. Conceptually, the specified flux condition q_0=$r(t)$ turns into a head condition when H_0 exceeds H_{po}. This can be expressed as a conventional stiff-spring boundary according to:

$$q_0 = \begin{cases} r(t) & H_0 \le H_{po}, \\ r(t) - k_{po}(H_0 - H_{po}), & H_0 > H_{po} \end{cases} \quad \text{(C.3)}$$

where k_{po} (s^{-1}) is the spring constant. The flux $-k_{po}$–$(H_0 - H_{po})$ reduces infiltration until the ponded boundary head is established.

The full atmospheric boundary condition results from combining the evaporation boundary Eq. (C.2) with the infiltration boundary Eq. (C.3), yielding:

$$q_0 = \begin{cases} -r(t)\tanh\left[\dfrac{\xi}{r(t)}(H_0 - H_{crit})\right], & r(t) < 0, \\ r(t)\mathfrak{H}(H_{p0} - H_0) + [r(t) - k_{po}(H_0 - H_{po})]\mathfrak{H}(H_0 - H_{po}), & r(t) \ge 0 \end{cases}, \quad \text{(C.4)}$$

where $\mathfrak{H}$ is the Heaviside step function [105].

Instead of the tan*h*-function in Eq. (C.4), COMSOL's smoothed version of the Heaviside function *flchhs* can be used. The inward recharge flux then becomes

$$q_0 = r(t)[-1 + 2\,flc2hs(H_0 - H_{crit}, \mathfrak{Q})], \quad r(t) < 0. \quad \text{(C.5)}$$

In Eq. (C.5) the transition zone is explicitly determined by the parameter $\mathfrak{Q}$ (m). However the slope of q_0 with respect to H_0 at H_{crit}, which is relevant for numerical stability, depends on H_{crit} and q_0.

Appendix D. Particle size distribution, surface area

It is generally accepted that the rate of mineral reactions is proportional to the area of the reacting surface [45,52]. In order to determine the macroscopic surface area a particle-size analysis was performed on washed residue sand (see Section 2.2 for details on washing procedure) using laser diffraction particle size analysis (LS 13 320 Beckman Coulter). In Fig. 18, the relative solid volume against particle diameter is displayed as the mean of four replicates.

With the assumption of spherical particles and a measured solid density of 2.74 g cm^{-3} the specific surface area of residue sand, as derived from the particle size distribution, amounts to 0.0264 m^2 g^{-1}.

References

[1] IAI International Aluminium Institute, Alumina production, 2011 (available from: http://world-aluminium.org/?pg=statistics, accessed 15.04.2011).
[2] CSIRO, Bauxite residue database, 2011 (available from: http://www.csiro.au/products/Bauxite-residue-database.html, accessed 15.04.2011).
[3] J.B. Wehr, I. Fulton, N.W. Menzies, Revegetation strategies for bauxite refinery residue: a case study of Alcan Gove in Northern Territory, Australia, Environ. Manage. 37 (2006) 297–306.
[4] ALCOA World Alumina, Dry stacking of bauxite residue, 2011 (available from: http://www.alcoa.com/global/en/environment/pdf/Dry_Stacking_Case_Study1.pdf, accessed 15.04.2011).
[5] G. Power, M. Gräfe, C. Klauber, Review of Current Bauxite Residue Management, Disposal and Storage: Practises, Engineering and Science, CSIRO Report, Australia, 2009.
[6] R.G. Courtney, S.N. Jordan, T. Harrington, Physico-chemical changes in bauxite residue following application of spent mushroom compost and gypsum, Land Degrad. Dev. 20 (2009) 572–581.
[7] R.G. Courtney, J.P. Timpson, Reclamation of fine fraction bauxite processing residue (red mud) amended with coarse fraction residue and gypsum, Water, Air, Soil Pollut. 164 (2004) 91–102.
[8] R.G. Courtney, J.P. Timpson, Nutrient status of vegetation grown in alkaline bauxite processing residue amended with gypsum and thermally dried sewage sludge—a two year field study, Plant Soil 266 (2004) 187–194.
[9] L.R. Hossner, R.H. Loeppert, Reclamation and Vegetation of Bauxite Residue Project Report to Aluminum Company of America, Soil & Crop Science Department Texas A&M University, Point Comfort, TX, USA, 1984.
[10] C. Thiyagarajan, I.R. Phillips, B. Dell, R.W. Bell, Micronutrient fractionation and plant availability in bauxite-processing residue sand, Aust. J. Soil Res. 47 (2009) 518–528.
[11] H.J. Woodard, L. Hossner, J. Bush, Ameliorating caustic properties of aluminum extraction residue to establish a vegetative cover, J. Environ. Sci. Health—Part A Toxic/Hazard. Substances Environ. Eng. 43 (2008) 1157–1166.
[12] R. Courtney, G. Mullen, T. Harrington, An evaluation of revegetation success on bauxite residue, Restoration Ecol. 17 (2009) 350–358.
[13] M.J. Gherardi, Z. Rengel, Bauxite residue sand has the capacity to rapidly decrease availability of added manganese, Plant Soil 234 (2001) 143–151.
[14] I.R. Phillips, C. Chen, Surface charge characteristics and sorption properties of bauxite-processing residue sand, Aust. J. Soil Res. 48 (2010) 77–87.
[15] B.E.H. Jones, R.J. Haynes, Bauxite processing residue: a critical review of its formation, properties, storage, and revegetation, Crit. Rev. Environ. Sci. Technol. 41 (2011) 271–315.
[16] C.R Chen, I.R. Phillips, L.L. Wei, Z.H. Xu, Behaviour and dynamics of diammonium phosphate in bauxite processing residue sand in Western Australia-II. Phosphorus fractions and availability, Environ. Sci. Pollut. Res. (2009) 1–9.
[17] C.R. Chen, I.R. Phillips, L.L. Wei, Z.H. Xu, Behaviour and dynamics of diammonium phosphate in bauxite processing residue sand in Western

Australia-I. NH3 volatilisation and residual nitrogen availability, Environ. Sci. Pollut. Res. (2009) 1–12.
[18] P.C. Lichtner, Continuum model for simultaneous chemical-reactions and mass-transport in hydrothermal systems, Geochim. Cosmochim. Acta 49 (1985) 779–800.
[19] P.C. Lichtner, Continuum formulation of multicomponent-multiphase reactive transport, in: P.C. Lichtner, C.I. Steefel, E.H. Oelkers (Eds.), Reactive Transport in Porous Media, Mineralogical Society of America, Washington DC, 1996, pp. 1–81.
[20] C.I. Steefel, New directions in hydrogeochemical transport modeling: incorporating multiple kinetic and equilibrium reaction pathways, in: L.R. Bentley, J.F. Sykes, C.A. Brebbia, W.G. Gray, G.F. Pinder (Eds.), Computational Methods in Water Resources, Balkema, Rotterdam, 2000, pp. 331–338.
[21] SteefelF C.I., D.J. DePaolo, P.C. Lichtner, Reactive transport modeling: an essential tool and a new research approach for the Earth sciences, Earth Planet. Sci. Lett. 240 (2005) 539–558.
[22] B. Hanson, J.W. Hopmans, J. Šimůnek, Leaching with subsurface drip irrigation under saline, shallow groundwater conditions, Vadose Zone J. 7 (2008) 810–818.
[23] B.R Hanson, J. Šimůnek, J.W. Hopmans, Evaluation of urea-ammonium-nitrate fertigation with drip irrigation using numerical modeling, Agric. Water Manage. 86 (2006) 102–113.
[24] A.I. Gärdenäs, J.W. Hopmans, B.R. Hanson, J. Šimůnek, Two-dimensional modeling of nitrate leaching for various fertigation scenarios under micro-irrigation, Agric. Water Manage. 74 (2005) 219–242.
[25] J. Šimůnek, D. Jacques, M.T. van Genuchten, D. Mallants, Multicomponent geochemical transport modeling using HYDRUS-1D and HP1, J. Am. Water Resour. Assoc. 42 (2006) 1537–1547.
[26] J. Šimůnek, S.A. Bradford, Vadose zone modeling: introduction and importance, Vadose Zone J. 7 (2008) 581–586.
[27] L. Wissmeier, D.A. Barry, Reactive transport in unsaturated soil: comprehensive modelling of the dynamic spatial and temporal mass balance of water and chemical components, Adv. Water Resour. 31 (2008) 858–875.
[28] L. Wissmeier, A. Brovelli, C. Robinson, F. Stagnitti, D.A. Barry, Pollutant fate and transport in the subsurface, in: Modelling of Pollutants in Complex Environmental Systems, ILM Publications, 2009, pp. 99–143.
[29] D.L. Parkhurst, C.A.J. Appelo, User's Guide to PHREEQC (Version 2): A Computer Program for Speciation, Batch-Reaction, One-Dimensional Transport, and Inverse Geochemical Calculations, U.S. Geological Survey, Denver, CO, USA, 1999.
[30] K. Snars, R.J. Gilkes, Evaluation of bauxite residues (red muds) of different origins for environmental applications, Appl. Clay Sci. 46 (2009) 13–20.
[31] S. Taylor, N. Pearson, Properties of Bayer process solids from Alcoa WA refineries and their component minerals. ALCOA World Alumina: Technology Delivery, Internal Report, 2001.
[32] B.I. Whittington, T.M. Fallows, M.J. Willing, Tricalcium aluminate hexahydrate (TCA) filter aid in the Bayer industry: factors affecting TCA preparation and morphology, Int. J. Miner. Process. 49 (1997) 1–29.
[33] B.I. Whittington, C.M. Cardile, The chemistry of tricalcium aluminate hexahydrate relating to the Bayer industry, Int. J. Miner. Process. 48 (1996) 21–38.
[34] S. Khaitan, D.A. Dzombak, G.V. Lowry, Chemistry of the acid neutralization capacity of bauxite residue, Environ. Eng. Sci. 26 (2009) 873–881.
[35] G.E. Ho, W.A. Robertson, G.I. Roach, A. Antonovsky, Morphological study of bayer process desilication product and its application to laboratory and plant digests, Ind. Eng. Chem. Res. 31 (1992) 982–986.
[36] J.L. Lowe, R.D. Hart, P.G. Smith, A.L. Rohl, G.M. Parkinson, Morphology and crystllinity: Insight into the mechanism of growth of DSP, in: 7th International Alumina Quality Workshop, CSIRO Minerals, Waterford,WA, Western Australia, 2005, pp. 168–173.
[37] T. Picaro, B. Pei, A.R. Kane, M.R. Thornber, A.B. Fletcher, Separation and mineralogical analysis of bayer red mud, Dev. Chem. Eng. Miner. Proces. 10 (2002) 475–489.
[38] P.G. Smith, R. Pennifold, T. Lwin, A. Kane, The composition of DSP formed under predesilication and high temperature Bayer digestion conditions, in: Light Metals: Proceedings of Sessions, in: TMS Annual Meeting, Warrendale, PA, USA, 2001, pp. 5–11.
[39] B. Whittington, T. Fallows, Formation of lime-containing desilication product (DSP) in the Bayer process: factors influencing the laboratory modelling of DSP formation, Hydrometallurgy 45 (1997) 289–303.
[40] B.I. Whittington, B.L. Fletcher, C. Talbot, The effect of reaction conditions on the composition of desilication product (DSP) formed under simulated Bayer conditions, Hydrometallurgy 49 (1998) 1–22.
[41] N.W. Menzies, I.M. Fulton, R.A. Kopittke, P.M. Kopittke, Fresh water leaching of alkaline bauxite residue after sea water neutralization, J. Environ. Qual. 38 (2009) 2050–2057.
[42] W. Stumm, J.J. Morgan, Aquatic Chemistry: Chemical Equilibria and Rates, Wiley, New York, 1996.
[43] J. Doherty, PEST Model-Independent Parameter Estimation User manual, fifth ed., Watermark Numerical Computing, Australia, 2004.
[44] M.R. Thornber, C.A. Hughes, The alkalinity of residues from Alcoa of Australia limited's refineries of south-west Australia, in: International Bauxite Tailings Workshop, Executive Management Services, Perth, Western Australia, 1992, pp. 136–147.
[45] J. Schott, O.S. Pokrovsky, E.H. Oelkers, The link between mineral dissolution/precipitation kinetics and solution chemistry, in: E.H. Oelkers, J. Schott (Eds.), 19th Annual V M Goldschmidt Conference, Mineralogical Society of America, Davos, Switzerland, 2009, pp. 207–258.
[46] N. Komada, E.F. Westrum, B.S. Hemingway, M.Y. Zolotov, Y.V. Semenov, I.L. Khodakovsky, L.M. Anovitz, Thermodynamic properties of sodalite at temperatures from 15 K to 1000 K, J. Chem. Thermodyn. 27 (1995) 1119–1132.
[47] R.L. Cooley, R.L. Naff, Regression modeling of ground-water flow, U.S. Geological Survey Open-File Report USGS-TWRI Book 3 Chapter B4, USGS Denver, CO, 1990, pp. 85–180.
[48] C. Amrhein, D.L. Suarez, Procedure for determining sodium-calcium selectivity in calcareous and gypsiferous soils, Soil Sci. Soc. Am. J. 54 (1990) 999–1007.
[49] J.H. Grove, C.S. Fowler, M.E. Sumner, Determination of the charge character of selected acid soils, Soil Sci. Soc. Am. J. 46 (1982) 32–38.
[50] D.L. Sparks, J.M. Bartels, J.M. Bigham, Part 3: Chemical Methods, Soil Science Scociety of America, Madison, WI, USA, 1996.
[51] AFNOR, NF X31-130, Détermination de la capacité d'échange cationique (CEC) et des cations extractibles, Paris, 1999.
[52] C.A.J. Appelo, D. Postma, Geochemistry Groundwater and Pollution, second ed., Balkema, Leiden, Netherlands, 2005.
[53] I.B. Oliveira, A.H. Demond, A. Salehzadeh, Packing of sands for the production of homogeneous porous media, Soil Sci. Soc. Am. J. 60 (1996) 49–53.
[54] Y. Mualem, New model for predicting hydraulic conductivity of unsaturated porous media, WRR 12 (1976) 513–522.
[55] M.T. van Genuchten, Closed-form equation for predicting the hydraulic conductivity of unsaturated soils, Soil Sci. Soc. Am. J. 44 (1980) 892–898.
[56] J. Šimůnek, M. Šejna, H. Saito, M. Sakai, M.T. van Genuchten, The HYDRUS-1D software package for simulating the movement of water, heat, and multiple solutes in variably saturated media Version 4.0, Department of Environmental Sciences, University of California Riverside, Riverside, CA, USA, 2009.
[57] M. Abramowitz, A.I. Stegun, Handbook of Mathematical Functions with Formulas, Graphs, and Mathematical Tables, United States Department of Commerce, National Bureau of Standards, Washington DC, 1972.
[58] O.A. Cirpka, P.K. Kitanidis, Numerical evaluation of solute dispersion and dilution in unsaturated heterogeneous media, WRR 38 (2002).
[59] T. Sato, H. Tanahashi, H.A. Loaiciga, Solute dispersion in a variably saturated sand, WRR 39 (2003).
[60] D. Schulze-Makuch, Longitudinal dispersivity data and implications for scaling behavior, Ground Water 43 (2005) 443–456.
[61] COMSOL Multiphysics®, 2011 (available from: http://www.comsol.com/, accessed 15.04.2011).
[62] S.R. Charlton, D.L. Parkhurst, Modules based on the geochemical model PHREEQC for use in scripting and programming languages, Comput. Geosci. (in press).
[63] MATLAB®, The MathWorks®, 2011 (available from: http://www.mathworks.com/, accessed 15.04.2011).
[64] H. Prommer, D.A. Barry, G.B. Davis, A one-dimensional reactive multicomponent transport model for biodegradation of petroleum hydrocarbons in groundwater, Environ. Modell.Software 14 (1999) 213–223.
[65] H. Prommer, D.A. Barry, C. Zheng, MODFLOW/MT3DMS-based reactive multicomponent transport modeling, Ground Water 41 (2003) 247–257.
[66] X. Mao, H. Prommer, D.A. Barry, C.D. Langevin, B. Panteleit, L. Li, Three-dimensional model for multi-component reactive transport with variable density groundwater flow, Environ. Modell. Software 21 (2006) 615–628.
[67] L. Wissmeier, D.A. Barry, Simulation tool for variably saturated flow with comprehensive geochemical reactions in two- and three-dimensional domains, Environ. Modell. Software 26 (2011) 210–218.
[68] E.P. Hodgkin, B.H. Hamilton, Fertilizers and eutrophication in Southwestern Australia—setting the scene, Fertilizer Res. 36 (1993) 95–103.
[69] J. Eastham, A simple water balance approach for estimating the amount of leachate from bauxite residue storage areas, ALCOA World Alumina, Internal Report, 2005.
[70] I.R. Phillips, Guidelines for constructing a field lysimeter to monitor water-nutrient-plant dynamics. ACOA World Alumina, Mining Environmental Group, Internal Report, 2009.
[71] G.H. Buchanan, G.B. Winner, The solubility of mono and diammonium phosphate, J. Ind. Eng. Chem. 12 (1920) 448–451.
[72] K. Bajracharya, D.A. Barry, Analysis of one-dimensional multispecies transport experiments in laboratory soil columns, Environ. Int. 21 (1995) 687–691.
[73] D.A. Barry, J.L. Starr, J.Y. Parlange, R.D. Braddock, Numerical analysis of the snow-plow effect, Soil Sci. Soc. Am. J. 47 (1983) 862–868.
[74] C.A.J. Appelo, Multicomponent ion exchange and chromatography in natural systems, in: P.C. Lichtner, C.I. Steefel, E.H. Oelkers (Eds.), Reactive Transport in Porous Media, Mineralogical Society of America, Washington, 1996, pp. 193–227.
[75] J.W.C. Wong, G.E. Ho, Effects of gypsum and sewage sludge amendment on physical properties of fine bauxite refining residue, Soil Sci. 152 (1991) 326–332.
[76] J.W.C. Wong, G.E. Ho, Use of waste gypsum in the revegetation on red mud deposits: a greenhouse study, Waste Manage. Res. 11 (1993) 249–256.
[77] R. Mattinson, Assessment of amendments for sand residue neutralization, Residue Neutralization. ALCOA World Alumina: Research and Development, Internal Report, 2003.
[78] D.A. Rose, F. Konukcu, J.W. Gowing, Effect of watertable depth on evaporation and salt accumulation from saline groundwater, Aust. J. Soil Res. 43 (2005) 565–573.

[79] E. Shimojima, R. Yoshioka, I. Tamagawa, Salinization owing to evaporation from bare-soil surfaces and its influences on the evaporation, J. Hydrol. 178 (1996) 109–136.
[80] C.E. Desborough, A.J. Pitman, P. Iranneiad, Analysis of the relationship between bare soil evaporation and soil moisture simulated by 13 land surface schemes for a simple non-vegetated site, Global Planet. Change 13 (1996) 47–56.
[81] C.M. Carter, H.A. van der Sloot, D. Cooling, A. van Zomeren, T. Matheson, Characterization of untreated and neutralized bauxite residue for improved waste management, Environ. Eng. Sci. 25 (2008) 475–488.
[82] B.I. Whittington, Quantification and characterisation of hydrogarnet and cancrinite present in desilication product by powder X-ray diffraction, 4th International Alumina Quality Workshop, 1996, 413–422.
[83] B.I. Whittington, The chemistry of CaO and $Ca(OH)_2$ relating to the Bayer process, Hydrometallurgy 43 (1996) 13–35.
[84] K.W. Perrott, Surface charge characteristics of amorphous aluminosilicates, Clays Clay Miner. 25 (1977) 417–421.
[85] D.A. Dzombak, F.M.M. Morel, Surface Complexation Modeling: Hydrous Ferric Oxide, Wiley, New York, 1990.
[86] Y. Watanabe, H. Yamada, J. Tanaka, Y. Komatsu, Y. Moriyoshi, Ammonium ion exchange of synthetic zeolites: the effect of their open-window sizes, pore structures, and cation exchange capacities, Sep. Sci. Technol. 39 (2004) 2091–2104.
[87] R.M Barrer, J. Klinowsk, H.S. Sherry, Zeolite exchangers—thermodynamic treatment when not all ions are exchangeable, J. Chem. Soc.,Faraday Trans. 69 (1973) 1669–1676.
[88] R.M. Barrer, R.P. Townsend, Ion-exchange equilibria in zeolites and clay-minerals—different concentration scales and derived thermodynamic functions, J. Chem. Soc., Faraday Trans. 80 (1984) 629–640.
[89] C. Colella, Ion exchange equilibria in zeolite minerals, Mineralium Deposita 31 (1996) 554–562.
[90] R.T. Pabalan, F.P. Bertetti, Cation-exchange properties of natural zeolites, Nat. Zeolites: Occurrence Prop. Appl. (2001) 453–518.
[91] J.W.C. Wong, G.E. Ho, Cation exchange behavior of bauxite refining residues from Western Australia, J. Environ. Qual. 24 (1995) 461–466.
[92] J. Anderson, R.W. Bell, I.R. Phillips, Mobility of cations in bauxite residue sand treated with residue fines, in: Joint Australian Society of Soil Science–New Zealand Society of Soil Science Conference, Massey, New Zealand, 2008.
[93] N.W. Menzies, I.M. Fulton, W.J. Morrell, Seawater neutralization of alkaline bauxite residue and implications for revegetation, J. Environ. Qual. 33 (2004) 1877–1884.
[94] C. Hanahan, D. McConchie, J. Pohl, R. Creelman, M. Clark, C. Stocksiek, Chemistry of seawater neutralization of bauxite refinery residues (red mud), Environ. Eng. Sci. 21 (2004) 125–138.
[95] J. Eastham, T. Morald, P. Aylmore, Effective nutrient sources for plant growth on bauxite residue: I. Comparing organic and inorganic fertilizers, Water Air Soil Pollut. 176 (2006) 5–19.
[96] R.D. Fuller, E.D.P. Nelson, C.J. Richardson, Reclamation of Red Mud (Bauxite Residues) using alkaline-tolerant grasses with organic amendments, J. Environ. Qual. 11 (1982) 533–539.
[97] J.W.C. Wong, G. Ho, Sewage-sludge as organic ameliorant for revegetation of fine bauxite refining residue, Resour., Conservation Recycl. 11 (1994) 297–309.
[98] J. Eastham, T. Morald, Effective nutrient sources for plant growth on bauxite residue: II. Evaluating the response to inorganic fertilizers, Water Air Soil Pollut. 171 (2006) 315–331.
[99] J.C. van Dam, R.A. Feddes, Numerical simulation of infiltration, evaporation and shallow groundwater levels with the Richards equation, J. Hydrol. 233 (2000) 72–85.
[100] E.G Lappala, R.W. Healy, E.P. Weeks, Documentation of Computer Program VS2D to Solve the Equations of Fluid Flow in Variably Saturated Porous Media, U.S. Geological Surfay, Denver, CO, USA, 1987.
[101] COMSOL Multiphysics®, Pesticide transport and reaction in soil, Earth Science Module Model Library, 2008.
[102] I. Kosztin, B. Barz, L. Janosi, Calculating potentials of mean force and diffusion coefficients from nonequilibrium processes without Jarzynski's equality, J. Chem. Phys. 124 (2006).
[103] J. Li, M. Hesse, J. Ziegler, A.W. Woods, An arbitrary Lagrangian Eulerian method for moving-boundary problems and its application to jumping over water, J. Comput. Phys. 208 (2005) 289–314.
[104] H.J. Vogel, O. Ippisch, Estimation of a critical spatial discretization limit for solving Richards' equation at large scales, Vadose Zone J. 7 (2008) 112–114.
[105] Wolfram MathWorld, Heaviside step function, 2011 (available from: http://mathworld.wolfram.com/HeavisideStepFunction.html, accessed 15.04.2011).